The Astrophysical Journal, 738:128 (20pp), 2011 September 10 doi:10.1088/0004-637X/738/2/128

ON THE CONSTANCY OF THE PHOTON INDEX OF X-RAY SPECTRA OF 4U 1728-34 THROUGH ALL SPECTRAL STATES

Elena Seifina[1] and Lev Titarchuk[2,3,4]
[1] Sternberg Astronomical Institute, Moscow State University, Universitetsky Prospect 13, Moscow 119992, Russia; seif@sai.msu.ru
[2] Dipartimento di Fisica, Università di Ferrara, Via Saragat 1, I-44100 Ferrara, Italy; titarchuk@fe.infn.it, lev@milkyway.gsfc.nasa.gov
[3] School of Physics, Astronomy, and Computational Sciences, George Mason University, Fairfax, VA 22030, USA
[4] Goddard Space Flight Center, NASA, code 663, Greenbelt, MD 20770, USA
Received 2011 January 5; accepted 2011 June 24; published 2011 August 18

ABSTRACT

We present an analysis of the spectral properties observed in X-rays from neutron star X-ray binary 4U 1728-34 during transitions between the low- and high-luminosity states when the electron temperature kT_e of the Compton cloud monotonically decreases from 15 to 2.5 keV. We analyze the transition episodes from this source observed with *BeppoSAX* and *RXTE* satellites. We find that the X-ray broadband energy spectra of 4U 1728-34 during all spectral states can be modeled by a combination of a thermal (blackbody-like) component, a Comptonized component (which we herein denote as *COMPTB*), and a Gaussian component. Spectral analysis using this model provides evidence that the photon power-law index Γ is almost constant ($\Gamma = 1.99 \pm 0.02$) when kT_e changes from 15 to 2.5 keV during these spectral transitions. We explain this quasi-stability of the index Γ by the model in which the spectrum is dominated by the strong thermal Comptonized component formed in the transition layer (TL) between the accretion disk and neutron star surface. The index quasi-stability takes place when the energy release in the TL is much higher than the flux coming to the TL from the accretion disk. Moreover, this index stability effect now established for 4U 1728-34 during spectral evolution of the source was previously suggested for a number of other neutron binaries. This intrinsic property of the neutron star is fundamentally different from that in black hole binary sources for which the index monotonically increases during spectral transition from the low state to the high state and saturates at high values of the mass accretion rate.

Key words: accretion, accretion disks – black hole physics – radiation mechanisms: non-thermal – stars: individual (4U 1728-34) – stars: neutron

Online-only material: color figures

1. INTRODUCTION

The evolution of spectral parameters of compact objects in X-ray binaries is of great interest for understanding the nature of compact objects. It is well known that a number of black hole (BH) candidate sources demonstrate correlations between their 1–10 Hz quasi-periodic oscillation (QPO) frequencies ν_L and photon power-law index Γ during spectral transition when sources evolve from the low state (LS) to the high state (HS), see Shaposhnikov & Titarchuk (2009), hereafter ST09. Then the definition of the spectral state is related to the level of soft blackbody emission presumably related to the mass accretion rate. In the HSs of BHs, these index-QPO frequency correlations sometimes show a saturation of Γ at high values of ν_L. On the other hand, ST09 (see also Titarchuk & Seifina 2009, hereafter TS09) found that Γ saturates with the mass accretion rate in almost any case of a BH binary. This saturation effect can be considered as a BH signature or as a signature of the converging flow (CF) into a BH (ST09 and TS09). The question that naturally arises is how the spectral index behaves as a function of the mass accretion rate or as a function of cutoff energy of the spectrum in neutron star (NS) sources.

Recently, Farinelli & Titarchuk (2011, hereafter FT11), collected X-ray spectra obtained by *BeppoSAX* from quite a few NS sources: Sco X-1, GX 17+2, Cyg X-2, GX 340+0, GX 3+1, and GS 1826-238. Their results probably indicate that the value of the photon index slightly varies around 2 independently of the spectral state (or electron temperature of a Compton cloud) at least for this particular sample of NS spectra (see Di Salvo et al. 2000; Farinelli et al. 2008). However, the available data for those sources were taken when these sources were in the HS or in the low state (LS), but nobody has analyzed up to now the spectral evolution from the LS to the HS for any particular NS source.

A suitable candidate for the study of the spectral evolution in an NS is the so-called atoll 4U 1728-34, which exhibits a remarkable spectral transition from the LS to the HS and vice versa. 4U 1728-34 (GX 354−0) was first resolved by *UHURU* scans of the Galactic center region in 1976 (see Forman et al. 1976 and Bradt et al. 1993). Then type I X-ray bursts from 4U 1728-34 were discovered during *SAS*-3 observations by Lewin et al. (1976) and Hoffman et al. (1976). Further, the bursting behavior was subsequently studied in detail using extensive observations by *SAS* 3, which accumulated 96 bursts in total. Using these data Basinska et al. (1984) presented evidence for a narrow distribution of peak burst fluxes, as well as a correlation between the peak flux and the burst phase. The distance to the source in the range of 4.2–6.4 kpc has been estimated by van Paradijs (1978) and confirmed by Basinska et al. (1984) and Kaminker et al. (1989) using measurements of the peak burst fluxes.

A radio counterpart of 4U 1728-34 was detected during Very Large Array (at 4.86 GHz) observations with a variable flux density in the range of ∼0.3–0.6 mJy (Marti et al. 1998). The estimated extinction of the source is $A_V \simeq 14$, and a precise position following from the detection of the radio counterpart allowed us to identify this source as a $K = 15$ infrared source (Marti et al. 1998). Long-term *Ariel-5* measurements, as well as extensive monitoring by the All-Sky Monitor (ASM) on board *RXTE*, suggest the presence of a long-term quasi-periodicity about 63–72 days (Kong et al. 1998). *RXTE*/Proportional

Counter Array (PCA) observations of the source in 1996 led to the discovery of nearly coherent millisecond oscillations during the X-ray bursts (Strohmayer et al. 1996).

Titarchuk & Osherovich (1999) presented a model for the radial oscillations and diffusion of the perturbation in the transition layer (TL) surrounding the NS. Using dimensional analysis, they identified the corresponding radial oscillation and diffusion frequencies in the TL with the low-Lorentzian ν_L and break frequencies ν_b for 4U 1728-34. They predicted values for ν_b, related to the diffusion in the boundary layer, that are consistent with the observed ν_b.

Subsets of the bursts observed during the PCA observations have also been studied by van Straaten et al. (2001) and Franco (2001) with particular attention to the relationship between the appearance of burst oscillations and a value of the mass accretion rate.

Titarchuk & Shaposhnikov (2005, hereafter TS05) analyzed *RXTE*/PCA observations of 4U 1728-34 in the energy range from 3 keV to 40 keV and found that, using the model comprising two Comptonization components (BMC[5]), the photon index Γ is consistent with being quasi-constant (around 2.2), while the low QPO frequency does not exceed 10 Hz. Γ then monotonically increases to values of 6. Moreover, using broadband observations of 4U 1728-34 by *BeppoSAX*, Di Salvo et al. (2000) and Piraino et al. (2000) fitted the X-ray spectra of 4U 1728-34 in a wide energy range from 0.1 keV to 200 keV by a sum of Blackbody components plus a thermal Comptonization spectrum, usually described by the XSPEC COMPTT model (Titarchuk 1994; Hua & Titarchuk 1995). The TS05 model cannot fit the *BeppoSAX* data; moreover, this model has more parameters than does the model of Di Salvo et al. (2000), Piraino et al. (2000), and FT11. Naturally, we pose the question of whether the FT11 model can fit the *BeppoSAX* along with *RXTE* data and what dependence of index versus spectral state can be found.

In this paper, we try to answer a fundamental question of the possibility of distinguishing a BH from NS systems, which others have extensively attempted to solve without considering the mass of the compact object as a main argument, in particular without using optical counterpart data to measure mass function. In this way, some methods have been proposed to identify systems that contain BHs using X-ray observational properties only. The strong rapid variability was first considered as a signature of the presence of BH (Oda et al. 1971), until the same rapid variability was detected in accreting NSs (Tennant et al. 1986). Now it is well established that Galactic BH candidates (BHCs) demonstrate two spectral states, the HS and LS, and transition between the two (Remillard & MacClintock 2006). However, sometimes the so-called atoll-NS sources[6] also show the "high" and "low" spectral states (D' Ai et al. 2006; TS05). Therefore, this property requires more detailed investigations of BHs versus NSs. Specifically, the HS spectra of BHCs are characterized by thermal emission at $\sim$1 keV, presumably originated in the accretion disk, along with a steep power-law tail whose photon index ($\Gamma = 2$–3) monotonically increases with the mass accretion rate (see ST09). The LS spectra show much weaker disk emission than that in the HS spectra and a harder power-law tail (the photon index of which is around $\Gamma \sim 1.7$). This hard component is generally believed to be a result of thermal Comptonization of soft (disk) photons in a hot gas (Compton cloud) in the vicinity of the compact object.

BHs, in contrast with NSs, sometimes demonstrate a more complicate X-ray spectrum. For example, the *RXTE* spectra of BH GRS 1915+105 require two Comptonization components, soft and hard ones (see Titarchuk & Seifina 2009). In this case one can clearly see the evolution of two photon indices $\Gamma_1 = 1.7$–3.0 and $\Gamma_2 = 2.7$–4.2 for the hard and soft components, respectively. Titarchuk & Seifina (2009) argued that the index saturation effect of the hard component is due to Comptonization of the soft (disk) photons in the CF into BH and that of the soft component is due to the thermal Comptonization in the TL when the mass accretion rate increases. These conclusions were later supported by Monte Carlo simulations by Laurent & Titarchuk (2011).

Moreover, in the description of BH and NS X-ray LS spectra with the thermal Comptonization model, there is an essential difference between these types of the compact sources. The electron temperature of the Compton (scattering) cloud kT_e is usually lower for NSs, $kT_e < 25$ keV, than that for BHs, $kT_e > 50$ keV (see Churazov et al. 1997). The lower electron temperature in NSs is a consequence of the additional cooling provided by the NS surface, which reflects X-ray photons and ultimately determines the value of the Compton cloud electron temperature (Titarchuk et al. 1998 and see also Sunyaev & Titarchuk 1989; Kluzniak 1993).

This fact of the observed difference between the BH and NSs was recently also discussed by Reynolds & Miller (2011). They conclude the observable difference of kT_e in these types of the sources is evidence of the absence and presence of a solid surface in BHs and NSs, respectively, and this fact can be considered as indirect evidence for the existence of the event horizon in BHs. It is worth pointing out that Titarchuk et al. (1998) and Titarchuk & Fiorito (2004) previously came to similar conclusions based on the analysis of the Compton cooling of the X-ray emission region (TL) in the presence (NS) and absence (BH) of the reflection surface.

Thus, the basic property that distinguishes BHs from NSs is the presence of the event horizon as well as a CF in the vicinity of a BH (Ebisawa et al. 1996). In fact, close to the event horizon, the strong gravitational force dominates the pressure forces and leads to an almost free fall CF of accreting material into a BH. The dynamic Comptonization of low energy photons off fast-moving electrons dominates the thermal Comptonization at a high-mass accretion rate and the plasma temperature of the CF is less than 10–15 keV; as a result, an extended steep power law is formed (see Titarchuk et al. 1997; Titarchuk & Zannias 1998; Laurent & Titarchuk 1999). These kinds of spectra are observed in the soft state of BH binaries (see, e.g., ST09 and TS09).

On the other hand, in NS sources the radiation pressure forces become dominant close to their surface; thus, a free fall should be suppressed at high-mass accretion rates. Does the presence of the firm surface in the NS make any difference in the dependence of the photon index Γ versus mass accretion rate with respect to that established in BHs (see ST09; TS09; ST10)? Furthermore, can the index saturation detected in many BHs with the mass accretion rate exist only in BH sources, since it has not yet been observed in NS sources? For example, Di Salvo et al. (2006), studying low-mass X-ray binaries hosting NSs, concluded that it is unlikely to distinguish BHs from NSs based on their X-ray spectra. However, FT11 argue that in NS sources the index Γ

[5] BMC is the so-called Bulk Motion Comptonization XSPEC Model (see details in Section 6.2.10 of "User's Guide of an X-Ray Spectral Fitting Package XSPEC v.12.6.0" and http://heasarc.gsfc.nasa.gov/xanadu/xspec/manual/Additive.html).

[6] Here, we use a term of the atoll-NS sources to specify NS X-ray binaries characterized by a specific "ϵ"-shaped track in a color–color diagram.

Table 1
List of *BeppoSAX* Observations of 4U 1728-34 Used in the Analysis

ObsID	Start Time (UT)	End Time (UT)	MJD Interval
20674001	1998 Aug 23 19:15:27	1998 Aug 24 09:14:15	51048.8–51049.4[1]
20889003	1999 Aug 19 02:01:32	1999 Aug 20 04:54:32	51409.1–51410.2[2]

References. [1] Di Salvo et al. 2000; [2] Piraino et al. 2000.

varies weakly until the soft photon illumination of the transition layer, Q_d, is much smaller than the energy release in the TL, $Q_{\rm cor}$. We try to test further this kind of index behavior in the NS source using X-ray observations of the atoll source 4U 1728-34 and compare it, if possible, with the index dependence on the mass accretion rate established in BHs.

In this paper, we present the analysis of the available *BeppoSAX* observations during 1998–1999 and *RXTE*/PCA/HEXTE observations during 1996–2000 for 4U 1728-34. In Section 2, we present the list of observations used in our data analysis, while in Section 3 we provide the details of X-ray spectral analysis. We analyze an evolution of X-ray spectral and timing properties during the state transition in Sections 4 and 5. We discuss our results and make our conclusions in Sections 6 and 7.

2. DATA SELECTION

Broadband energy spectra of the source were obtained combining data from three *BeppoSAX* Narrow Field Instruments (NFIs): the Low Energy Concentrator Spectrometer (LECS; Parmar et al. 1997) for 0.3–4 keV, the Medium Energy Concentrator Spectrometer (MECS; Boella et al. 1997) for 1.8–10 keV, and the Phoswich Detection System (PDS; Frontera et al. 1997) for 15–60 keV. The SAXDAS data analysis package was used for processing data. For each of the instruments we performed the spectral analysis in the energy range for which the response matrix is well determined. The LECS data were renormalized based on MECS. Relative normalization of the NFIs was treated as free parameters in model fitting, except for the MECS normalization that was fixed at a value of 1. After the fitting procedure we checked whether these normalizations were in a standard range for each instrument.[7]

Specifically, the LECS/MECS renormalization ratio is 0.92, and the PDS/MECS renormalization ratio is 0.97. In addition, spectra were rebinned according to energy resolution of the instruments in order to obtain significant data points. We rebinned the LECS spectra, applying a rebinning template for grouping (lecs_2.grouping) with an energy-dependent binning factor used in GRPPHA of XSPEC.[8] We also rebinned the PDS spectra with a linear binning factor of two, grouping two bins together (resulting bin width is 1 keV). In Table 1 we list the *BeppoSAX* observations used in our analysis.

We also analyzed the available data obtained with *RXTE* (Bradt et al. 1993), which were found in the time period from 1996 February to 2000 July (see also the review by Galloway et al. 2008). In our investigation we selected 127 observations made at different count rates (luminosity states) with a good coverage of rise–decay flare track. We performed an analysis of *RXTE* observations of 4U 1728-34 during four years for eight intervals, indicated by blue rectangles in Figure 1 (top). We also analyzed two *BeppoSAX* observations, whose dates are marked by green triangles in Figure 1.

Standard tasks of the HEASOFT/FTOOLS 5.3 software package were utilized for data processing. For spectral analysis we used PCA *Standard 2* mode data, collected in the 3–20 keV energy range. The standard dead time correction procedure was applied to the data. The average dead time correction is in the range 3%–10% depending on the count rate value.

HEXTE data were used in order to construct broadband spectra. We subtracted the background corrected in off-source observations. To exclude the channels with the largest uncertainties, we used only data in the 20–60 keV energy range for the spectral analysis. The HEXTE data were renormalized based on the PCA. Typical PCA/HEXTE renormalization factor is 0.98. We used the data that are available through the GSFC public archive (http://heasarc.gsfc.nasa.gov). In Table 2 we list the groups of *RXTE* observations that cover the source evolution from quiescent to flare events.

Note that we did not use any normalization factor to normalize between *BeppoSAX* and *RXTE* data. We also used public 4U 1728-34 data from the ASM on board *RXTE*. We retrieved the ASM light curves (in the 2–12 keV energy range) from the public *RXTE*/ASM archive at MIT.[9] In the bottom panel of Figure 1 we show a mean count rate (blue dashed line) during the 1996–2010 interval of ASM/*RXTE* monitoring observations of 4U 1728-34. In this panel one can also see a long-term quasi-periodic variability of mean soft flux during a cycle of $\sim$ six years. We investigate available periods of slow variability (indicated by green) during which we also have the *BeppoSAX* observations of 4U 1728-34 (see also the upper panel of Figure 1).

We use definitions of the low- and high-luminosity states to relate these states to the source luminosity, and we demonstrate that during the high–low state transition the electron temperature of the Compton cloud changes from 2.5 keV to 15 keV, and vice versa, respectively. Thus, the "high spectral state" corresponds to the "low electron temperature state" and vice versa the "low spectral state" corresponds to the "high electron temperature state." During the flare seen in the ASM light curve the electron temperature kT_e usually decreases from 15 keV to 2.5 keV. We introduce a definition of a "burst" to point out a significant increase in X-ray flux (about a factor of five) with respect to the persistent emission level. Specifically, we identify a "burst" when the ASM count rate is greater than 10 counts s^{-1}. We associate the count rate increase with the increase in the mass accretion rate.

3. SPECTRAL ANALYSIS

In our spectral data analysis we use a model that consists of a sum of the Comptonization (*COMPTB*) component (*COMPTB* is the XSPEC Contributed model;[10] see Farinelli et al. 2008,

[7] http://heasarc.nasa.gov/docs/sax/abc/saxabc.html
[8] http://heasarc.gsfc.nasa.gov/FTP/sax/cal/responses/grouping
[9] http://xte.mit.edu/ASM_lc.html
[10] http://heasarc.gsfc.nasa.gov/docs/software/lheasoft/xanadu/xspec/models/comptb.html

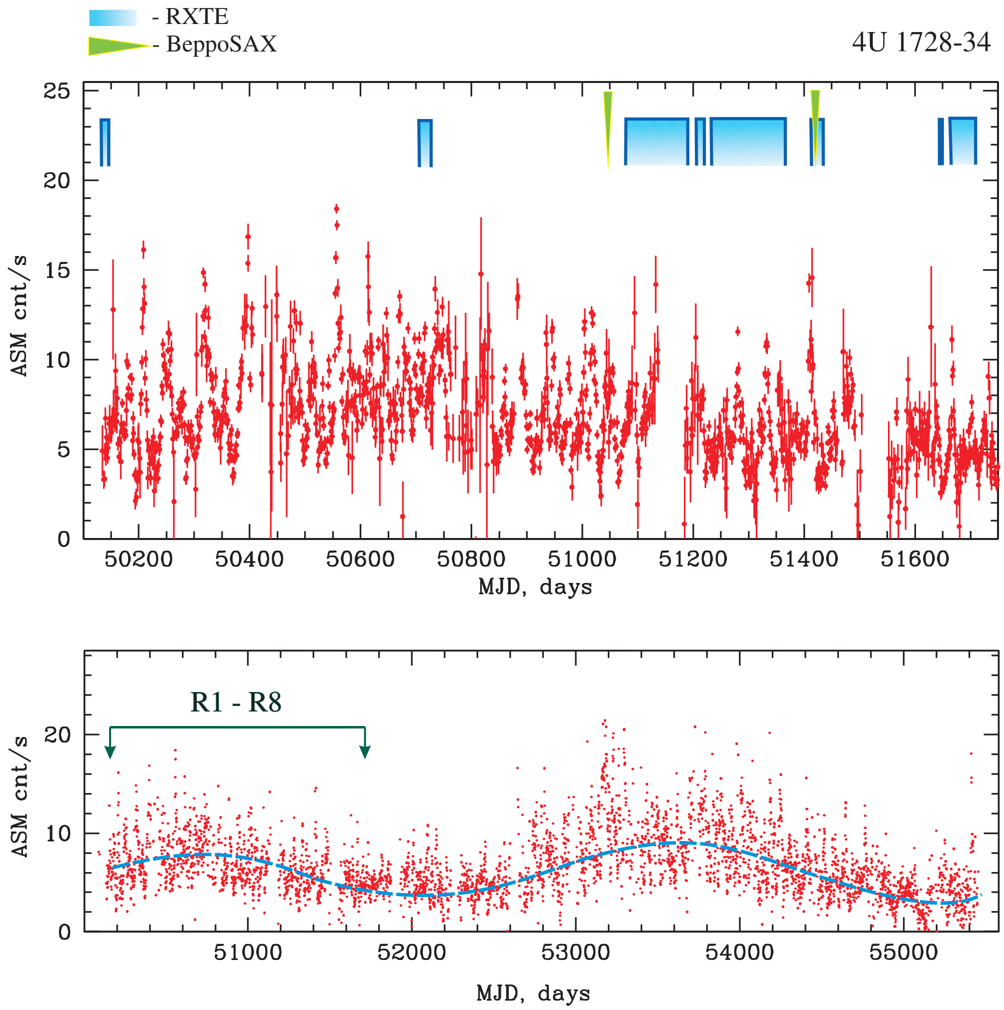

Figure 1. Top: evolution of the ASM/*RXTE* count rate during 1996–2006 observations of 4U 1728-34. Blue rectangles indicate the *RXTE*/PCA & HEXTE data of pointed observations, and green triangles show *BeppoSAX* NFI data used for analysis. Bottom: ASM/*RXTE* 1 day-type light curve of 4U 1728-34 during 1996–2010. The blue dashed line shows a mean count rate and indicates the long-term quasi-periodic variability of mean soft flux during a cycle of ∼ six years. The green double arrow points out the 1996–2000 time interval of *RXTE* observations used in our analysis (see R1–R8 intervals).

(A color version of this figure is available in the online journal.)

Table 2
List of Groups of the *RXTE* Observation of 4U 1728-34 Used in the Analysis

Number of Set	Dates (MJD)	*RXTE* Proposal ID	Dates (UT)	Rem.	Ref.
R1	50128–50143	10073	1996 Feb 15–Mar 1		1, 2, 3, 4, 5, 7, 8
R2	50710–50728	20083	1997 Sep 19–Oct 1		3, 4, 5, 7, 8
R3	51086–51196	30042	1998 Sep 30–1999 Jan 18		4
R4	51409–51443	40019	1999 Aug 19–Sep 22	*BeppoSAX*	8
R5	51237–51359	40027	1999 Feb 27–Jul 10		6, 8
R6	51198–51213	40033	1999 Jan 20–Feb 4		6, 8
R7	51667–51733	50023	2000 Mar 7–Jul 8		6, 8
R8	51652–51657	50029	2000 Apr 18–23		6, 8

References. (1) Strohmayer et al. 1996; (2) Ford & van der Klis 1998; (3) van Straaten et al. 2001; (4) Di Salvo et al. 2001; (5) Mendez et al. 2001; (6) Migliari et al. 2003; (7) Jonker et al. 2000; (8) TS05.

hereafter F08), a soft blackbody component of temperature $T_{\rm BB}$, and the Gaussian line component. The *COMPTB* spectral component has the following parameters: temperature of the seed photons T_s, energy index of the Comptonization spectrum α $(=\Gamma-1)$, electron temperature T_e, Comptonization fraction f $(f = A/(1+A))$, and the normalization of the seed photon spectrum $N_{\rm COMPTB}$ (see the Appendix for the definition of $N_{\rm COMPTB}$).

In Figure 2 we illustrate our spectral model as a basic model for fitting the *BeppoSAX* and *RXTE* spectral data for 4U 1728-34. We assume that accretion onto an NS takes place when the material passes through the main two regions, a geometrically thin accretion disk (standard Shakura–Sunyaev disk; see Shakura & Sunyaev 1973), and the TL, where NS and disk soft photons are upscattered off hot electrons. In other words, in our picture, the emergent thermal Comptonization

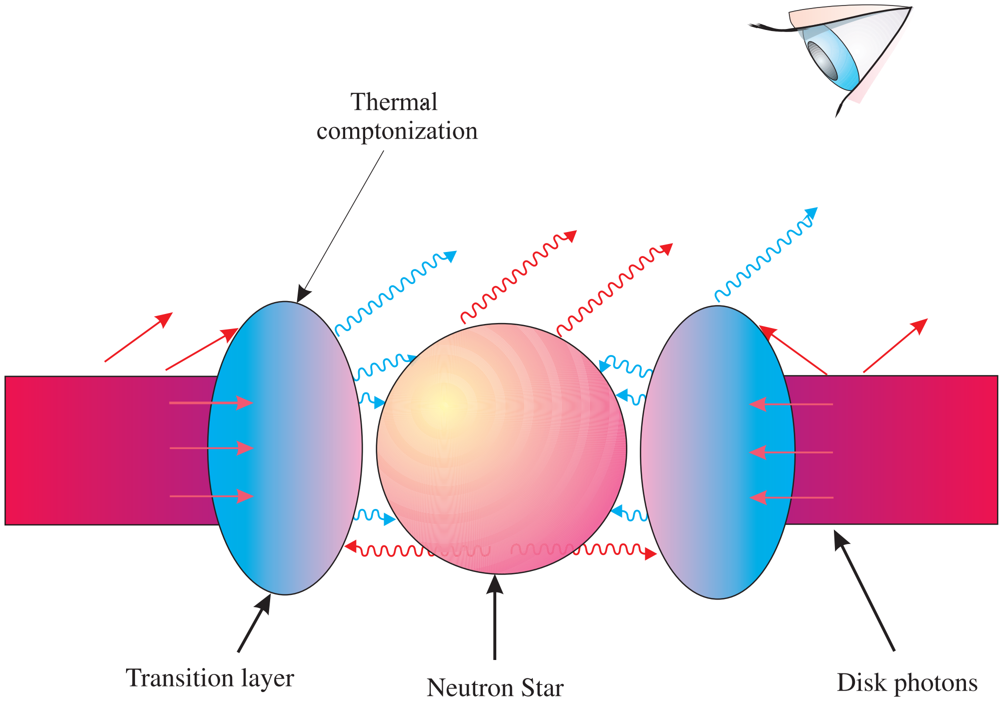

Figure 2. Suggested geometry of the system. Disk and NS soft photons are upscattered (Comptonized) in the relatively hot plasma of the TL (between the accretion disk and the NS surface). Some fraction of these photons is seen directly by the Earth observer. Red and blue photon trajectories correspond to soft and hard (upscattered) photons, respectively.

(A color version of this figure is available in the online journal.)

spectrum is formed in the TL region, where disk BB-like seed photons and NS soft photons are upscattered in the relatively hot plasma. Some fraction of these seed soft photons can also be seen directly by the Earth observer. Red and blue photon trajectories shown in Figure 2 correspond to soft (seed) and hard (upscattered) photons, respectively.

We show examples of X-ray spectra in Figure 3 (for *BeppoSAX* data) and in Figures 4 and 5 (for *RXTE* data). Spectral analysis of *BeppoSAX* and *RXTE* observations indicates that X-ray spectra of 4U 1728-34 can be described by the model, while its Comptonization component can be presented by the *COMPTB* model. Moreover, for broadband *BeppoSAX* observations, this spectral model component is modified by photoelectric absorption at low energies. Also following the suggestions of Di Salvo et al. (2000) and Piraino et al. (2000), we add a *Gaussian* line at ~6.7 keV and a thermal blackbody component at low energies (1–4 keV) to improve the fit statistics. Along with these components, Di Salvo et al. (2000) included a narrow *Gaussian* line to fit an excess in the residuals around 1.7 keV. We also test the presence of this line feature, but the addition of this component to the model does not improve the quality of the model fit. It is worth noting that D' Ai et al. (2006) analyzed simultaneous *Chandra* and *RXTE* observations of 4U 1728-34 (2002 March 2–5). They fitted the 1.2–35 keV continuum spectrum with a blackbody plus a Comptonized component, and they fitted large residuals at 6–10 keV by a broad (FWHM ~ 2 keV) Gaussian emission line or, alternatively, by two absorption edges associated with low ionized iron and Fe XXV/XXVI. However, in the framework of this model, D' Ai et al. (2006) found no evidence of broad or narrow Fe K lines between 6 and 7 keV. However, using our model *wabs*(blackbody+COMPTB+Gaussian)* we found an iron line feature during all *BeppoSAX* and *RXTE* observations.

On the top of Figure 3 we demonstrate the best-fit *BeppoSAX* spectrum using our model, and in the bottom right panel we show the best-fit spectrum along with $\Delta\chi$ for the model (reduced $\chi^2 = 1.16$ for 445 dof). In particular, we find that the addition of the soft blackbody-like component of temperature $T_{\rm BB} = 0.5$–0.7 keV to the model significantly improves the fit quality of the *BeppoSAX* spectra. The line emission is clearly detected in the range from 5 to 8 keV, as one can see from the left bottom panel of Figure 3. We show that this line is quite broad, and it is much wider than the instrumental response whose width is smaller than 0.02 keV.[11] Thus, we include in the model a simple *Gaussian* component whose parameters are a centroid line energy $E_{\rm line}$, the width of the line $\sigma_{\rm line}$, and the normalization $N_{\rm line}$ to fit the data in the 6–8 keV range. We also include in the model the interstellar absorption with a column density $N_{\rm H}$. It should be mentioned that we fixed certain parameters of the *COMPTB* component: $\gamma = 3$ (low energy index of the seed photon spectrum) and $\delta = 0$ because we neglect the efficiency of the bulk inflow effect versus the thermal Comptonization in the case of NS source 4U 1728-34.

For the *BeppoSAX* data (see Tables 1 and 3) we find that the spectral index α is of 1.03 ± 0.04 (or the corresponding photon index $\Gamma = \alpha + 1$ is 2.03 ± 0.04). While the temperature of the seed photons T_s of the *COMPTB* component changes from 1.2 to 1.3 keV, the color temperature of the soft *Blackbody* component $T_{\rm BB}$ is around 0.6 keV.

Unfortunately, *RXTE* detectors cannot provide well-calibrated spectra below 3 keV, while the broad energy band of *BeppoSAX* telescopes allows us to determine the parameters of *blackbody* components at soft energies. Thus, in order to fit the *RXTE* data we have to fix the temperature of the *blackbody* component at a value of $T_{\rm BB} = 0.7$ keV, obtained as an upper

[11] See ftp://heasarc.gsfc.nasa.gov/sax/cal/responses/98_11.

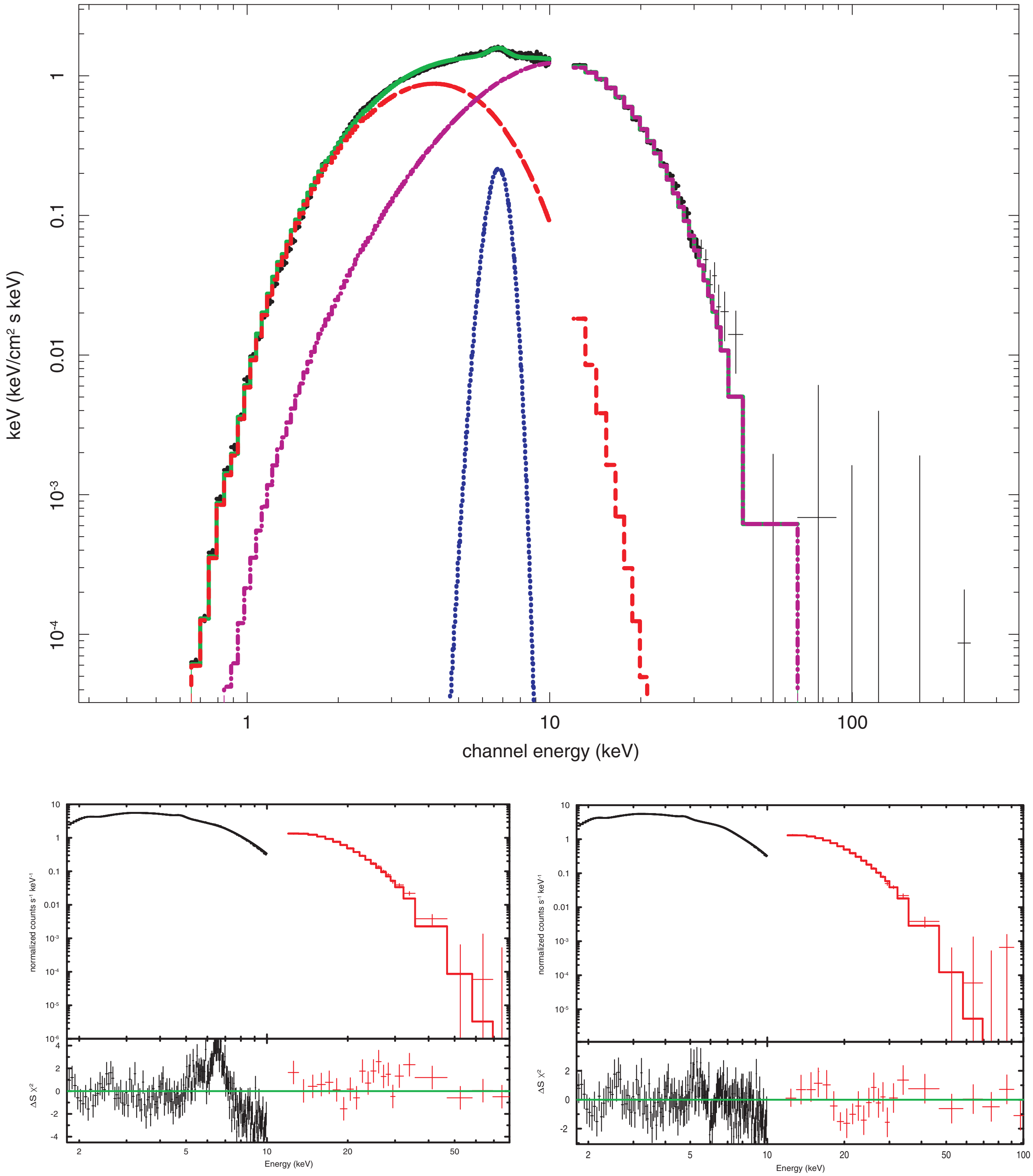

Figure 3. Top: best-fit spectrum of 4U 1728-34 in $E * F(E)$ units using *BeppoSAX* observation 20889003 carried out on 1999 April 19. The data are presented by crosses and the best-fit spectral model *wabs*(blackbody+COMPTB+Gaussian)* by the green line. The model components are shown by red, crimson, and blue lines for *blackbdody*, *COMPTB*, and *Gaussian* components, respectively. Bottom panels: spectrum in units of counts along with $\Delta\chi$. Left bottom panel: best-fit spectrum and $\Delta\chi$ for the model fit without the line component (reduced $\chi^2 = 2.15$ for 445 dof). Right bottom panel: same as that on the left one but with the addition of the *Gaussian* (K_α-line) component (reduced $\chi^2 = 1.16$ for 445 dof). The best-fit model parameters are $\Gamma = 2.07 \pm 0.04$, $T_e = 3.29 \pm 0.04$ keV, $E_{\rm line} = 6.0 \pm 0.1$ keV, and $\mathrm{EW}_{\rm line} = 51 \pm 11$ eV (see more details in Table 3).

(A color version of this figure is available in the online journal.)

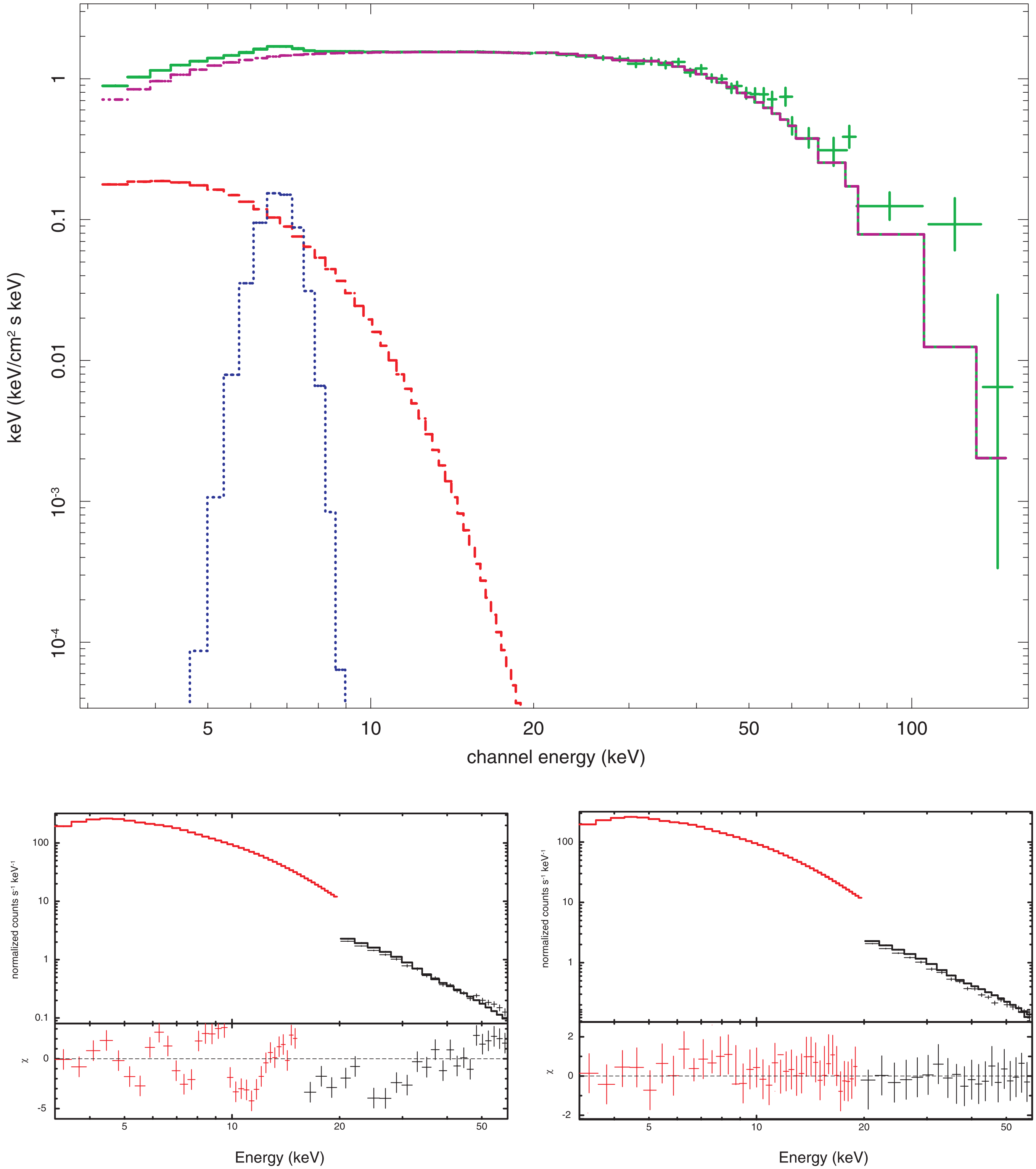

Figure 4. Best-fit *RXTE* spectrum of 4U 1728-34 for the low-luminosity state in units $E * F(E)$ (top) and the spectra in count units (bottom panels) with $\Delta\chi$ for the 30042-03-01-00 observation. Left bottom panel: fit of the model *wabs* $*$ *COMPTB*, ($\chi^2_{\rm red} = 2.1$ for 61 dof). Right bottom panel: same as the latter one but with the addition of an iron *Gaussian* line and the *blackbody* component, namely, using the model *wabs* $*$ (*blackbody* + *COMPTB* + *Gaussian*) ($\chi^2_{\rm red} = 1.18$ for 57 dof). The best-fit model parameters are $\Gamma = 1.99 \pm 0.02$, $T_e = 10.4 \pm 0.3$ keV, and $E_{\rm line} = 6.54 \pm 0.03$ keV (see more details in Table 4). Red, violet, and blue lines stand for *blackbody*, *COMPTB*, and *Gaussian* components, respectively.

(A color version of this figure is available in the online journal.)

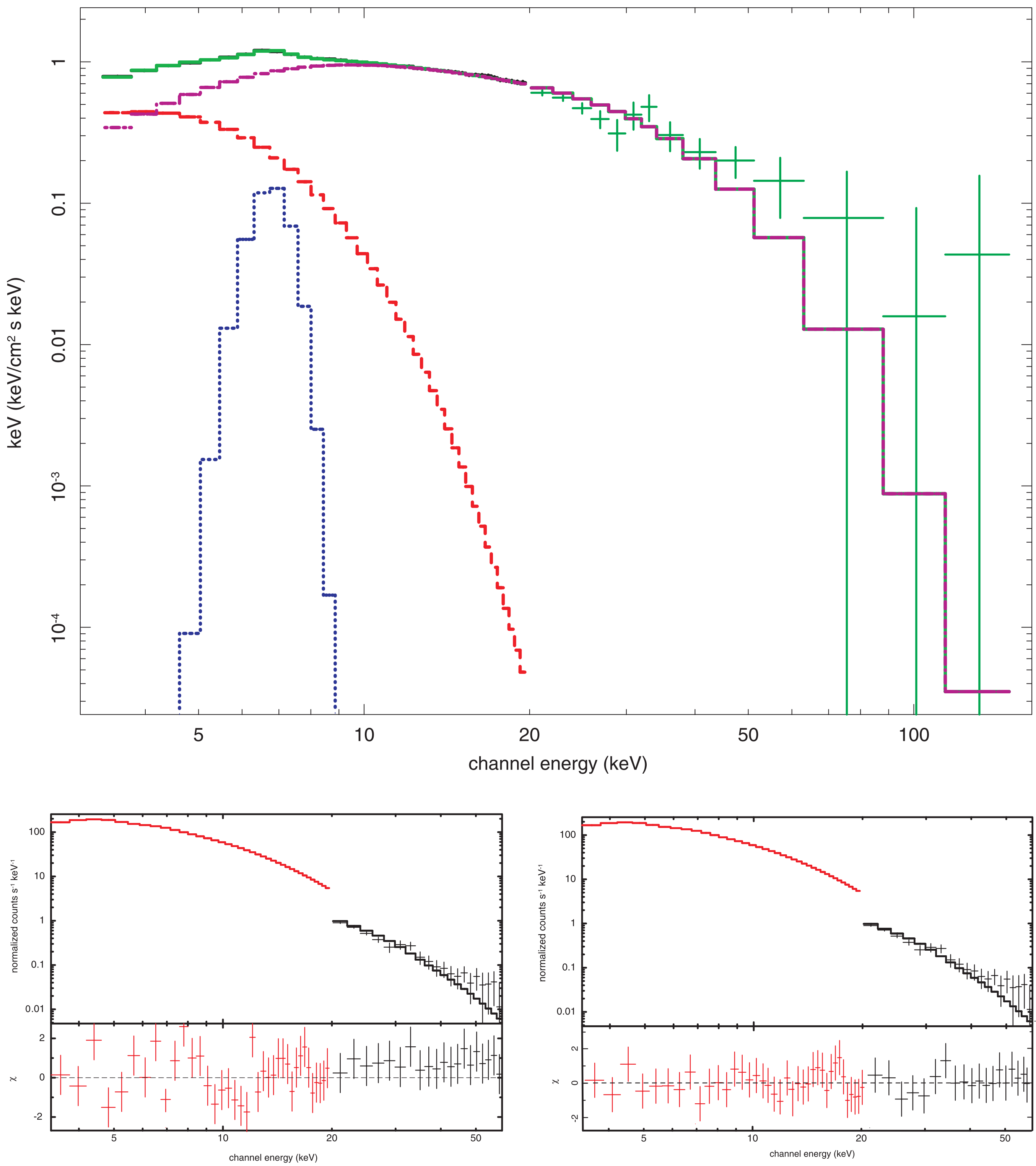

Figure 5. Best-fit *RXTE* spectrum of 4U 1728-34 for the high-luminosity state in units $E * F(E)$ (top) and the spectra in count units (bottom panel) with $\Delta\chi$ for the 50023-01-12-00 observation. Left bottom panel: fit of the model *wabs* ∗ *COMPTB* ($\chi^2_{\rm red} = 1.79$ for 61 dof). Right bottom panel: same as the latter one but with the addition of an iron *Gaussian* line and the *Blackbody* component, namely, using the model *wabs* ∗ (*blackbody* + *COMPTB* + *Gaussian*) ($\chi^2_{\rm red} = 1.2$ for 57 dof). The best-fit model parameters are $\Gamma = 1.99 \pm 0.03$, $T_e = 5.5 \pm 0.1$ keV, and $E_{\rm line} = 6.75 \pm 0.04$ keV (see more details in Table 4). Red, violet, and blue lines stand for *Blackbody*, *COMPTB*, and *Gaussian* components, respectively.

(A color version of this figure is available in the online journal.)

limit in our analysis of the *BeppoSAX* data. The best-fit spectral parameters using *RXTE* observations are presented in Table 4. In particular, we find that electron temperature T_e of the *COMPTB* component varies from 2.5 to 15 keV, while photon index Γ is almost constant ($\Gamma = 1.99 \pm 0.02$) for all observations. It is worth noting that the width $\sigma_{\rm line}$ of the *Gaussian* component does not vary much and is in the range of 0.3–0.6 keV. Color temperature T_s of the *COMPTB* component is around 1.3 keV,

Table 3
Best-Fit Parameters of the Spectral Analysis of *BeppoSAX* Observations of 4U 1728-34 in the 0.3–60 keV Energy Range[a]

Observational ID	MJD (day)	T_{BB} (keV)	N_{BB}[b]	T_s (keV)	$\alpha = \Gamma - 1$	T_e (keV)	log(*A*)	N_{COMPTB}	E_{line} (keV)	N_{line}[b]	EW_{line} (eV)	χ^2_{red} (dof)
20674001	51048.70	0.47(3)	2.65(2)	1.30(3)	0.99(7)	3.76(8)	0.10(4)	4.18(3)	7.4(1)	0.55(4)	52(16)	1.25(457)
20889003	51409.50	0.62(5)	1.61(1)	1.21(5)	1.07(4)	3.29(4)	1.06(6)	3.56(2)	6.0(1)	0.43(4)	51(11)	1.16(445)

Notes. Parameter errors correspond to the 1σ confidence level.
[a] The spectral model is *wabs* $*$ (*blackbody* + *COMPTB* + *Gaussian*), normalization parameters of *blackbody* and *COMPTB* components are in units of L_{37}/d_{10}^2 erg^{-1} s^{-1} kpc^{-2}, where L_{37} is the source luminosity in units of 10^{37} erg s^{-1}, d_{10} is the distance to the source in units of 10 kpc, and the *Gaussian* component is in units of 10^{-2} $\times$ total photons cm^{-2} s^{-1} in line.

which is consistent with that using the *BeppoSAX* data set of our analysis (Table 3) and previous studies by Di Salvo et al. (2000) and Piraino et al. (2000).

We fixed the value of the *COMPTB* parameter log(*A*) to 1 when the best-fit values of log(*A*) $\gg$ 1, because in any case of log(*A*) $\gg$ 1 a Comptonization fraction $f = A/(1 + A)$ is approximately 1 and variations of $A \gg 1$ do not further improve the fit quality. We use a value of hydrogen column $N_H = 2.73 \times 10^{22}$ cm^{-2}, which was found by Piraino et al. (2000). A systematic error of 0.5% has been applied to all analyzed *RXTE* spectra.

In Figure 4 we show an example of the best-fit *RXTE* spectrum of 4U 1728-34 for the low-luminosity state in units of $E * F(E)$ (top) and the spectrum in count units (bottom panels) with $\Delta\chi$ for the 30042-03-01-00 observation. On the left bottom panel we demonstrate a fit of the model *wabs* $*$ *COMPTB* ($\chi^2_{red} = 2.1$ for 61 dof) and on the right, the same as the latter one, adding an iron *Gaussian* line and the *blackbody* component using the model *wabs* $*$ (*blackbody* + *COMPTB* + *Gaussian*) for which we obtain $\chi^2_{red} = 1.18$ for 57 dof. The best-fit model parameters for this observation are $\Gamma = 1.99 \pm 0.02$, $T_e = 10.4 \pm 0.3$ keV, and $E_{line} = 6.54 \pm 0.03$ keV (see more details in Table 4). Red, violet, and blue lines denote *blackbody*, *COMPTB*, and *Gaussian* components, respectively. We also apply the same procedure to the spectrum during the high-luminosity state, and in Figure 5 we present the results for the 50023-01-12-00 observation. On the left bottom panel we show a fit of the model *wabs* $*$ *COMPTB* ($\chi^2_{red} = 1.79$ for 61 dof) and on the right we present the same as the latter one, adding an iron *Gaussian* line and the *blackbody* components using the model *wabs* $*$ (*blackbody* + *COMPTB* + *Gaussian*), for which $\chi^2_{red} = 1.2$ for 57 dof. The best-fit model parameters in this case are $\Gamma = 1.99 \pm 0.02$, $T_e = 5.5 \pm 0.1$ keV, and $E_{line} = 6.75 \pm 0.04$ keV (see more details in Table 4).

The adopted spectral model shows a very good performance throughout all data sets used in our analysis. Namely, the value of reduced $\chi^2_{red} = \chi^2/N_{dof}$, where N_{dof} is the number of degrees of freedom (dof), is around 1.0 or less for most observations. For a small fraction (less than 3%) of spectra with high counting statistics χ^2_{red} reaches 1.5. However, it never exceeds a rejection limit of 1.7. Note that the energy range for the cases, in which we obtain the poor fit statistic (2 among 127 spectra with $\chi^2 = 1.7$ for 44 dof), is related to the iron line region. It is possible that the shape of the Fe line is more complex than a simple Gaussian (i.e., there may be a blend of different energies, the presence of an edge, or broadening by Comptonization). The fits tend to favor a broad line (see Table 4), which might be caused by Comptonization. However, this possible complexity is not well constrained by our data.

Moreover, recent analysis of high-resolution *XMM-Newton* spectra of 4U 1728-34 (Ng et al. 2010; Egron et al. 2011) using different spectral models also reveals evident residuals at 6–7 keV, which are attributed to the presence of a broad iron emission line. This feature can be fitted equally well by a composition of the pure iron line and the corresponding absorption edge as well as *Laor* instead of the *Gaussian* line profile (Ng et al. 2010) and also by a relativistically smeared line component or by a relativistically smeared reflection model component (Egron et al. 2011). This variety of the line models used in the data analysis for 4U 1728-34 demonstrates complexity of the line appearance in this source.

It is worth noting that we find some differences between our values for the best-fit model parameters and those in the literature. In particular, the photon index Γ, estimated by Di Salvo et al. (2000) for ObsID = 20674001, is 1.60 ± 0.25 while our value of $\Gamma = 1.9 \pm 0.2$. This difference in the index values can be explained using slightly different models. Di Salvo et al. (2000) included a narrow *Gaussian* line around 1.7 keV (radiative recombination emission from Mg XI) in order to fit an excess of the residuals of the continuum model. However our model result, using the *BeppoSAX* observation (ID = 20889003), confirms the result of Piraino et al. (2000), although we apply a slightly different spectral model. Our best-fit photon index $\Gamma = 1.9 \pm 0.2$ is very close to that obtained by Piraino et al. (2000) using the best-fit parameters of the COMPTT model (see Titarchuk 1994) electron temperature $kT_e = 3.16 \pm 0.03$ keV and optical depth (for spherical geometry) $\tau_0 = 11.4 \pm 0.2$.

Using broadband *BeppoSAX* observations we can well determine all parameters of our spectral model, while due to the extensive observations of 4U 1728-34 by *RXTE* we are able to investigate the overall pattern of the source behavior during the spectral transitions in the 3–60 keV energy range.

4. EVOLUTION OF X-RAY SPECTRAL PROPERTIES DURING SPECTRAL STATE TRANSITIONS

We have established common characteristics of the rise–decay spectral transition of 4U 1728-34 based on their spectral parameter evolution of X-ray emission in the energy range from 3 to 60 keV using *RXTE*/PCA and HEXTE data. In Figures 4 and 5 we present typical examples of the *RXTE* LS and HS spectra for 4U 1728-34. In fact, one can clearly see from these figures that the normalization of the thermal (blackbody-like) component is a factor of two higher in the HS than that in the LS, although photon indices Γ for each of these spectra are slightly variable from 1.8 to 2.1, mostly concentrated around $\Gamma = 2$ (see that distribution of Γ on the left-hand panel of Figure 6).

We test the hypothesis of $\Gamma_{appr} \approx 2$ using χ^2-statistic criterion. We show the distribution of $\chi^2_{red}(\Gamma_{appr}) = \frac{1}{N}\sum_{i=1}^{N}\left(\frac{\Gamma_i - \Gamma_{appr}}{\Delta\Gamma_i}\right)^2$ versus Γ_{appr} in the right-hand panel of

Table 4
Best-Fit Parameters of the Spectral Analysis of PCA & HEXTE/*RXTE* Observations of 4U 1728-34 in the 3–60 keV Energy Range[a]

Observational ID	Start Time (MJD)	Exposure Time (s)	Rate (counts s^{-1})	$\alpha = \Gamma - 1$	T_e (keV)	$\log(A)$[b]	N_{COMPTB}[c]	N_{Bbody}[c]	E_{line} (keV)	N_{line}[c]	EW_{line} (eV)	χ^2_{red} (dof)	F_1/F_2[d]
10073-01-01-00	50128.49	9632	1824	0.98(6)	3.54(3)	0.8(1)	3.4(1)	2.4(2)	6.6(1)	1.2(1)	100(30)	1.16(64)	2.82/1.43
10073-01-01-000	50128.494	12180	1752	1.00(3)	3.71(4)	0.7(1)	3.4(2)	2.09(4)	6.68(8)	0.7(1)	106(20)	1.1(64)	2.69/1.49
10073-01-02-00	50129.27	9488	2071	1.00(2)	2.91(2)	1.00[b]	4.05(6)	2.85(5)	6.63(1)	0.57(1)	120(20)	0.98(65)	3.26/1.31
10073-01-02-000	50129.27	9840	1927	1.11(7)	3.18(7)	0.94(6)	3.7(2)	2.56(2)	6.64(3)	0.73(2)	110(20)	1.28(64)	3.03/1.34
10073-01-03-000	50129.66	11550	2040	1.02(3)	3.16(4)	0.41(3)	4.53(5)	3.19(2)	6.58(2)	0.32(1)	150(20)	1.39(64)	3.21/1.28
10073-01-03-00	50129.93	9488	2071	1.05(4)	3.17(4)	0.41(4)	4.56(7)	3.28(2)	6.58(7)	0.30(1)	130(10)	1.15(64)	3.22/1.27
10073-01-04-000	50131.46	12540	1493	0.99(2)	4.64(3)	0.2(1)	3.25(2)	2.67(2)	6.53(5)	0.38(1)	90(10)	1.32(64)	2.08/1.46
10073-01-04-00	50131.79	9664	1387	0.95(2)	5.2(1)	0.18(5)	3.12(3)	2.36(3)	6.50(3)	0.32(1)	90(10)	1.07(64)	2.08/1.46
10073-01-06-000	50135.48	4160	994	0.91(7)	8.1(3)	0.27(2)	2.3(2)	1.19(3)	6.50(2)	0.30(2)	50(8)	1.4(64)	1.45/1.60
10073-01-06-00	50135.78	9600	1021	0.90(8)	8.2(2)	0.30(2)	2.34(6)	1.18(2)	6.51(2)	0.31(1)	40(10)	1.1(64)	1.43/1.71
10073-01-08-000	50136.88	14560	1035	0.90(9)	8.6(3)	0.33(1)	2.32(4)	1.05(1)	6.50(3)	0.32(1)	40(10)	1.12(64)	1.50/1.81
10073-01-07-000	50136.89	16000	972	0.86(3)	8.4(1)	0.29(2)	2.25(5)	1.06(3)	6.48(5)	0.31(1)	40(10)	0.96(64)	1.41/1.73
10073-01-07-00	50137.22	2992	1058	0.98(2)	8.5(4)	0.39(3)	2.43(6)	1.05(2)	6.45(4)	0.33(2)	40(10)	1.17(64)	1.54/1.76
10073-01-08-00	50138.06	7888	1030	0.89(9)	8.1(2)	0.31(2)	2.39(3)	1.07(1)	6.60(2)	0.32(1)	40(10)	1.56(64)	1.49/1.75
10073-01-09-000	50138.86	16510	1090	0.91(8)	8.4(1)	0.33(1)	2.51(2)	1.08(3)	6.48(3)	0.34(1)	50(10)	1.54(64)	1.58/1.89
10073-01-09-00	50139.20	7968	1095	0.82(9)	6.9(1)	0.18(1)	2.66(3)	1.64(2)	6.62(2)	0.16(1)	70(10)	1.05(64)	1.73/1.74
10073-01-10-01	50143.00	12530	1191	0.99(2)	12.2(3)	0.84(1)	2.40(4)	0.92(3)	6.61(5)	0.44(5)	50(20)	1.09(64)	1.49/2.46
20083-01-01-00	50710.24	9520	2013	1.0(2)	3.01(4)	0.59(5)	3.8(3)	2.75(6)	6.6(1)	0.5(2)	120(20)	0.86(57)	4.65/4.3
20083-01-01-01	50710.51	4464	2043	0.99(7)	2.96(5)	0.4(1)	5.0(3)	2.01(2)	6.7(1)	1.0(1)	160(30)	0.79(57)	3.33/1.2
20083-01-01-02	50711.31	4928	1998	1.00(5)	2.89(3)	0.6(1)	4.65(4)	2.6(3)	6.7(1)	0.5(1)	110(20)	0.8(57)	3.25/1.17
20083-01-01-020	50712.24	11500	1183	0.99(7)	3.02(4)	0.3(1)	4.3(3)	2.1(1)	6.58(8)	0.33(8)	110(10)	1.15(57)	3.03/1.15
20083-01-02-000	50712.35	3264	1908	1.00(5)	3.06(2)	0.28(5)	4.2(1)	2.3(1)	6.5(1)	0.6(3)	130(10)	0.81(57)	3.09/1.14
20083-01-02-01	50712.65	12770	1657	1.00(8)	3.02(3)	0.3(1)	4.6(1)	2.1(2)	6.6(1)	0.3(1)	130(8)	0.89(57)	3.27/1.20
20083-01-03-00	50714.98	3520	2281	0.99(9)	2.96(2)	0.5(2)	5.45(3)	2.8(6)	6.7(1)	0.4(1)	140(10)	0.72(57)	3.71/1.36
20083-01-03-000	50715.01	15650	2431	1.12(9)	2.85(2)	1.00[b]	5.69(8)	2.19(1)	6.7(1)	0.3(1)	130(10)	0.93(58)	3.96/1.44
20083-01-04-00	50717.51	16780	1644	0.99(4)	3.22(7)	0.15(5)	3.5(3)	2.2(1)	6.59(9)	0.33(9)	100(10)	0.92(57)	2.65/1.01
20083-01-04-01	50718.38	16420	1388	0.99(2)	4.21(8)	0.09(3)	3.1(1)	1.85(9)	6.5(1)	0.5(3)	90(10)	1.39(57)	2.19/1.10
20083-01-03-02	50721.18	6736	1002	0.99(3)	3.02(3)	0.28(4)	3.54(3)	2.15(6)	6.5(1)	0.4(1)	100(10)	0.87(57)	2.57/0.95
20083-01-03-020	50721.19	12580	999	0.99(7)	2.96(4)	0.4(1)	3.51(4)	2.17(3)	6.6(1)	0.28(9)	100(10)	0.96(57)	2.56/0.95
20083-01-04-02	50722.25	3360	936	0.99(6)	2.95(4)	0.8(2)	3.1(1)	2.4(3)	6.7(1)	0.3(1)	90(10)	0.73(57)	2.39/0.88
20083-01-04-020	50722.26	16540	1511	0.99(6)	3.08(5)	0.3(1)	3.4(2)	2.1(1)	6.6(1)	0.3(1)	100(10)	0.98(57)	2.45/0.92
30042-03-01-00	51086.30	8432	1795	0.99(2)	10.4(3)	0.71(3)	3.92(5)	0.99(8)	6.54(3)	0.61(1)	50(20)	1.21(57)	2.62/3.67
30042-03-02-00	51093.21	9712	2421	0.97(5)	3.16(4)	0.41(5)	5.35(8)	3.34(4)	6.53(2)	0.55(2)	140(8)	1.29(57)	3.90/1.60
30042-03-01-01	51109.94	1920	1528	0.94(3)	11.1(6)	1.0(2)	3.19(2)	1.05(9)	6.58(8)	0.53(7)	30(20)	1.1(57)	2.19/3.44
30042-03-02-01	51110.01	2352	1525	0.85(9)	9.6(2)	0.52(4)	3.52(3)	0.93(2)	6.53(4)	0.49(3)	40(20)	0.96(57)	2.19/3.39
30042-03-03-01	51110.08	4624	1584	0.89(9)	9.8(2)	0.60(3)	3.64(4)	0.85(2)	6.55(3)	0.49(2)	40(20)	1.06(57)	2.28/3.48
30042-03-04-00	51113.01	6608	1583	0.85(8)	9.6(1)	0.50(2)	3.85(2)	1.12(3)	6.55(2)	0.49(2)	40(20)	1.07(57)	2.27/3.54
30042-03-01-03	51112.94	2048	1589	0.86(9)	9.7(2)	0.56(4)	3.79(5)	0.89(2)	6.54(2)	0.52(3)	60(20)	1.22(57)	2.29/3.56
30042-03-01-04	51115.07	3312	1599	0.85(9)	9.9(2)	0.53(3)	3.68(2)	0.94(3)	6.53(2)	0.51(2)	50(20)	1.07(57)	2.29/3.64
30042-03-05-00	51115.14	6672	1595	0.88(7)	10.2(1)	0.69(3)	3.52(4)	0.92(1)	6.57(3)	0.54(2)	70(20)	0.93(57)	2.28/3.60
30042-03-07-01	51119.94	3376	1719	0.89(9)	9.6(2)	0.53(2)	4.03(3)	0.9(2)	6.50(1)	0.47(2)	70(10)	0.92(57)	2.48/3.73
30042-03-07-00	51120.00	6752	1670	0.88(6)	9.6(1)	0.59(2)	3.92(2)	0.89(4)	6.53(4)	0.51(2)	70(20)	1.15(57)	2.40/3.66
30042-03-08-00	51122.17	5296	1637	0.89(7)	10.10(2)	0.67(3)	3.67(3)	0.92(3)	6.57(1)	0.55(2)	50(30)	1.09(57)	2.40/3.66
30042-03-10-00	51127.77	4432	1787	0.93(3)	8.2(2)	0.46(2)	4.35(3)	1.19(3)	6.51(2)	0.52(2)	60(20)	1.3(57)	2.62/3.34
30042-03-10-01	51127.88	2656	1730	0.92(2)	7.9(2)	0.51(6)	3.96(8)	1.13(4)	6.53(4)	0.69(9)	50(30)	0.88(57)	2.54/3.17
30042-03-11-00	51127.93	1013	1752	0.96(3)	8.4(3)	0.55(3)	4.07(3)	1.15(2)	6.46(2)	0.75(5)	70(30)	0.95(57)	2.58/3.23
30042-03-12-00	51128.60	16640	1776	0.98(2)	7.95(9)	0.52(2)	4.14(4)	1.21(2)	6.49(4)	0.69(4)	60(30)	0.97(57)	2.63/3.08
30042-03-13-00	51128.93	9824	1765	0.99(1)	8.13(9)	0.53(4)	4.09(2)	1.23(2)	6.47(3)	0.72(5)	80(30)	0.76(57)	2.61/3.08
30042-03-14-02	51133.27	880	2059	0.9(1)	4.4(1)	0.3(3)	4.73(3)	2.71(2)	6.49(5)	0.57(7)	160(20)	0.93(57)	3.23/1.88
30042-03-14-01	51133.34	2432	2033	1.00(9)	4.46(7)	0.3(3)	4.61(5)	2.72(9)	6.62(3)	0.54(4)	150(20)	1.12(57)	3.18/1.04
30042-03-14-00	51133.41	2160	2194	0.99(6)	4.09(2)	0.3(2)	5.12(4)	2.97(8)	6.60(3)	0.62(4)	160(20)	1.18(57)	3.46/1.90
30042-03-15-00	51133.55	13700	1989	1.00(3)	4.79(3)	0.3(1)	4.5(2)	2.71(4)	6.55(6)	0.55(2)	120(20)	1.3(57)	3.10/1.90
30042-03-16-00	51134.00	14940	1787	1.00(5)	5.48(3)	0.35(5)	4.28(7)	2.32(4)	6.54(1)	0.55(2)	120(20)	0.96(57)	3.75/2.10
30042-03-17-00	51134.54	3200	1686	1.00(3)	6.9(2)	0.40(8)	3.91(6)	1.79(7)	6.54(4)	0.55(4)	120(20)	1.2(57)	3.75/2.10
30042-03-18-00	51193.32	9488	1232	0.997(9)	14.4(3)	1.07(1)	2.58(3)	0.97(6)	6.49(2)	0.60(3)	30(20)	1.12(57)	1.78/2.79
30042-03-19-01	51195.20	2432	1253	1.000(8)	14.3(5)	1.01(1)	2.47(4)	0.95(9)	6.53(2)	0.54(2)	40(20)	1.15(57)	1.82/2.83
30042-03-19-00	51195.26	9568	1286	0.99(3)	14.1(3)	0.96(5)	2.58(3)	0.9(1)	6.54(1)	0.55(1)	50(20)	0.94(57)	1.86/2.90
30042-03-20-00	51196.94	4608	1365	0.99(4)	12.06(4)	0.83(6)	3.13(2)	0.90(6)	6.51(2)	0.56(2)	50(10)	1.21(57)	1.98/2.95
40033-06-01-00	51198.12	10030	1124	0.99(7)	13.3(3)	1.00[b]	2.87(3)	0.86(2)	6.67(1)	0.30(4)	70(8)	1.29(58)	1.99/3.20
40033-06-02-00	51200.19	9792	1219	0.99(5)	9.8(2)	0.61(3)	3.35(4)	0.75(4)	6.63(1)	0.43(4)	60(10)	1.16(57)	2.20/2.94
40033-06-02-01	51201.91	16420	1293	0.99(6)	7.93(8)	0.44(2)	3.89(2)	1.04(3)	6.64(2)	0.40(4)	60(8)	1.04(57)	2.37/2.68

Table 4
(Continued)

Observational ID	Start Time (MJD)	Exposure Time (s)	Rate (count s^{-1})	$\alpha = \Gamma - 1$	T_e (keV)	$\log(A)$[b]	$N_{\rm COMPTB}$[c]	$N_{\rm Bbody}$[c]	$E_{\rm line}$ (keV)	$N_{\rm line}$[c]	$EW_{\rm line}$ (eV)	$\chi^2_{\rm red}$ (dof)	F_1/F_2[d]
40033-06-02-03	51203.98	13230	1084	1.00(3)	5.44(3)	0.35(6)	4.33(8)	1.98(4)	6.66(3)	0.36(1)	40(10)	1.07(57)	2.64/2.08
40033-06-02-04	51205.92	6576	1685	0.99(4)	5.43(5)	0.33(7)	4.3(1)	1.96(5)	6.65(2)	0.38(2)	40(10)	0.96(57)	2.63/2.06
40033-06-02-07	51206.06	2784	1634	0.99(2)	5.81(9)	0.32(9)	4.2(1)	1.88(3)	6.61(3)	0.35(3)	40(10)	0.98(57)	2.54/2.07
40033-06-02-05	51206.12	2704	1716	1.00(3)	5.37(6)	0.4(1)	4.3(2)	1.73(8)	6.64(3)	0.44(3)	50(10)	0.87(57)	2.68/2.06
40033-06-02-06	51206.19	3120	996.9	1.00(4)	5.55(8)	0.4(1)	3.8(1)	1.89(3)	6.69(5)	0.49(3)	50(10)	1.19(57)	2.45/1.92
40033-06-03-00	51207.18	3264	1491	1.00(2)	6.6(2)	0.35(7)	3.69(6)	1.48(6)	6.61(3)	0.39(3)	30(10)	1.19(57)	2.30/2.12
40033-06-03-06	51207.27	864	911.7	1.00(3)	6.8(3)	0.8(1)	3.5(1)	1.33(9)	6.58(6)	0.39(6)	40(10)	1.2(57)	2.22/2.10
40033-06-03-01	51208.92	6608	1207	0.99(2)	5.91(7)	0.31(6)	3.68(8)	1.74(6)	6.69(2)	0.33(2)	30(10)	0.97(57)	2.28/1.88
40033-06-03-02	51210.12	1856	1635	0.99(3)	4.27(3)	0.24(6)	3.81(5)	2.16(6)	6.68(3)	0.41(4)	40(10)	1.16(57)	2.62/1.49
40033-06-03-07	51211.78	2368	1379	1.00(2)	5.46(9)	0.34(9)	3.4(1)	1.98(4)	6.74(3)	0.35(3)	30(10)	0.93(57)	2.15/1.64
40033-06-03-03	51211.91	12350	1112	1.00(1)	5.71(5)	0.30(6)	3.37(7)	1.54(3)	6.68(1)	0.36(1)	30(10)	1.37(57)	2.10/1.64
40033-06-03-05	51213.91	5152	1601	0.99(3)	3.98(2)	0.25(6)	3.74(5)	2.07(4)	6.68(2)	0.39(2)	30(10)	1.32(57)	2.58/1.59
40027-06-01-01	51237.04	4528	1023	1.06(2)	7.8(3)	0.59(2)	2.38(4)	0.78(2)	6.56(4)	0.54(4)	70(10)	1.17(57)	1.58/1.57
40027-06-01-02	51237.18	3360	1087	0.99(3)	7.3(2)	0.38(8)	2.69(6)	0.89(4)	6.57(3)	0.38(3)	40(10)	0.74(57)	1.67/1.66
40027-06-01-04	51238.36	3392	851.8	0.99(1)	7.9(3)	0.39(7)	2.42(4)	0.84(2)	6.51(3)	0.39(3)	40(10)	1.09(57)	1.68/1.65
40027-06-01-05	51238.49	2720	1044	0.91(9)	8.2(4)	0.36(4)	2.46(5)	0.86(2)	6.58(3)	0.41(3)	50(10)	1.72(57)	1.57/1.85
40027-06-01-06	51238.56	2720	1110	0.97(4)	8.3(4)	0.37(6)	2.63(4)	0.85(4)	6.60(3)	0.32(3)	40(10)	0.91(57)	1.68/1.88
40027-06-01-03	51238.76	9616	1054	0.999(9)	9.6(2)	0.43(3)	2.45(3)	0.73(3)	6.61(1)	0.31(1)	40(10)	0.95(57)	1.60/1.93
40027-06-01-07	51239.90	3200	657.9	0.99(2)	8.9(3)	0.41(7)	2.41(3)	0.85(6)	6.62(3)	0.30(2)	40(10)	1.13(57)	1.58/1.82
40027-06-01-08	51240.04	1136	1270	1.00(4)	7.1(3)	0.36(9)	3.1(1)	0.94(3)	6.72(3)	0.21(3)	40(10)	1.09(57)	1.95/1.99
40027-08-01-02	51359.15	1056	934.7	1.00(4)	7.2(3)	0.2(1)	2.89(4)	1.47(4)	6.58(5)	0.29(4)	40(10)	0.93(57)	1.81/1.69
40019-03-02-02	51409.17	1984	2078	1.00(3)	3.02(3)	0.52(8)	5.7(2)	3.16(6)	6.64(3)	0.64(3)	100(20)	1.37(57)	4.43/1.71
40019-03-02-01	51409.23	2400	2102	0.94(6)	3.04(6)	0.32(7)	6.7(1)	3.5(3)	6.67(3)	0.39(4)	150(10)	1.09(57)	4.47/1.71
40019-03-02-00	51409.55	14370	1268	0.94(7)	2.94(2)	0.43(5)	7.54(9)	3.1(2)	6.64(2)	0.59(2)	170(8)	1.12(57)	5.09/1.95
40019-03-03-01	51410.16	2048	1911	0.96(8)	2.87(5)	0.8(1)	7.36(7)	3.2(1)	6.62(4)	0.44(2)	160(10)	1.07(57)	5.20/2.18
40019-03-03-00	51410.23	11760	2321	0.99(3)	3.02(2)	0.40(4)	7.21(6)	3.16(4)	6.62(1)	0.53(2)	170(6)	1.05(57)	4.95/1.87
40019-03-01-03	51442.39	8800	438.6	1.00(6)	5.7(3)	0.3(1)	2.6(1)	2.7(6)	6.64(6)	0.28(2)	40(10)	0.83(57)	1.72/1.35
40019-03-01-07	51442.49	1200	457.6	0.99(5)	5.6(2)	0.3(1)	2.6(1)	2.6(3)	6.75(6)	0.22(2)	40(10)	1.09(57)	1.74/1.36
40019-03-01-04	51442.60	1440	692.9	0.99(4)	5.3(2)	0.3(1)	2.7(1)	2.1(4)	6.73(5)	0.28(4)	40(10)	1.53(57)	1.79/1.33
40019-03-01-01	51442.67	1152	705.3	1.01(6)	5.2(1)	0.4(1)	3.0(1)	2.7(6)	6.69(5)	0.26(4)	40(5)	1.17(57)	1.83/1.33
40019-03-01-02	51442.74	848	708.7	1.00(4)	5.4(2)	0.4(2)	3.0(1)	5.5(2)	6.70(7)	0.21(4)	40(8)	1.34(57)	1.84/1.36
40019-03-01-00	51442.80	12610	758.2	0.99(3)	4.57(8)	0.26(9)	3.0(1)	2.9(2)	6.73(1)	0.26(4)	40(10)	1.28(57)	1.99/1.25
40019-03-01-06	51443.19	6288	759.2	0.99(2)	4.80(5)	0.24(9)	3.1(1)	3.4(4)	6.72(3)	0.23(2)	40(10)	0.91(57)	2.06/1.33
50023-01-01-00	51610.70	2656	551.7	0.95(3)	10.07(6)	0.63(6)	4.04(5)	0.93(5)	6.56(3)	0.46(3)	50(8)	1.03(57)	1.99/2.83
50023-01-02-00	51613.69	2544	801.5	0.96(4)	10.4(2)	1.00(1)	2.93(4)	0.85(4)	6.62(3)	0.45(3)	50(10)	1.52(57)	1.98/2.74
50023-01-03-00	51615.89	3376	788.8	0.89(6)	8.5(2)	0.40(2)	3.21(3)	0.9(3)	6.56(3)	0.36(3)	40(8)	1.75(57)	1.96/2.55
50023-01-04-00	51619.81	3296	520	0.93(3)	7.8(3)	0.42(4)	2.96(4)	1.07(5)	6.58(3)	0.35(3)	40(10)	1.07(57)	1.91/2.21
50023-01-05-00	51622.81	3328	773.5	0.94(6)	6.7(3)	0.22(2)	3.49(3)	3.69(4)	5.99(7)	0.07(1)	30(10)	0.76(57)	1.98/1.89
50023-01-06-00	51625.73	2992	536.6	0.98(7)	5.5(2)	0.32(5)	3.11(5)	1.5(2)	6.58(4)	0.31(3)	40(8)	1.04(57)	2.04/1.56
50023-01-07-00	51628.85	2928	1896	0.97(9)	4.1(2)	0.05(5)	6.5(1)	3.9(2)	6.73(2)	0.72(3)	150(6)	0.88(57)	4.01/2.02
50029-23-01-00	51652.4	2256	280.5	1.00(3)	13.6(8)	0.7(1)	1.4(2)	0.63(4)	6.50(5)	0.29(3)	40(10)	1.2(57)	1.03/1.44
50029-23-01-01	51652.46	2224	417.3	0.89(6)	9.9(5)	0.34(5)	1.68(4)	0.62(6)	6.54(5)	0.19(3)	30(10)	0.91(57)	1.04/1.42
50029-23-02-00	51657.13	2464	906.8	0.89(3)	8.7(4)	0.39(3)	2.17(5)	0.68(5)	6.57(3)	0.27(3)	40(10)	0.95(57)	1.38/1.77
50029-23-02-01	51657.19	2480	1027	0.97(6)	7.8(3)	0.46(4)	2.51(6)	0.9(1)	6.63(3)	0.26(3)	40(8)	1.29(57)	1.57/1.80
50029-23-02-02	51657.58	5664	773.8	0.96(2)	7.9(2)	0.38(2)	2.49(3)	1.2(2)	6.62(2)	0.27(2)	40(10)	0.94(57)	1.52/1.72
50029-23-02-03	51657.73	7408	384.3	0.99(8)	8.6(2)	0.40(4)	2.28(4)	1.3(3)	6.58(2)	0.26(2)	40(10)	0.81(57)	1.43/1.64
50023-01-12-00	51663.96	1792	1195	0.99(3)	5.5(1)	0.3(1)	2.9(1)	2.6(4)	6.75(4)	0.28(3)	40(10)	1.2(57)	1.90/1.43
50023-01-13-00	51667.55	2592	1715	1.02(4)	2.95(4)	0.48(9)	3.8(1)	2.3(3)	6.64(3)	0.36(3)	50(8)	1.1(57)	2.88/1.08
50023-01-14-00	51669.55	2528	961.9	1.0(2)	4.07(9)	0.2(4)	3.07(6)	2.95(9)	6.72(5)	0.27(3)	40(6)	1.24(57)	2.01/1.06
50023-01-15-00	51673.61	2048	313.9	1.00(4)	10.1(6)	0.47(9)	1.73(3)	0.74(4)	6.51(4)	0.25(4)	40(10)	1.09(57)	1.16/1.42
50023-01-17-00	51679.72	2688	368.7	1.01(6)	9.4(4)	0.6(1)	2.15(4)	0.40(5)	6.55(4)	0.32(3)	50(10)	0.78(57)	1.41/1.74
50023-01-18-00	51682.51	2656	372.2	0.89(6)	7.9(3)	0.32(3)	2.61(3)	1.5(4)	6.63(5)	0.23(4)	40(10)	0.92(57)	1.55/1.86
50023-01-19-00	51685.50	2720	632.4	0.97(5)	7.3(2)	0.35(3)	2.8(3)	1.9(2)	6.70(4)	0.26(3)	40(6)	0.81(57)	1.72/1.76
50023-01-20-00	51688.76	2608	613.7	0.94(4)	8.1(3)	0.38(3)	2.67(5)	1.0(3)	6.57(4)	0.28(3)	50(8)	0.92(57)	1.63/1.92
50023-01-21-00	51691.71	3056	654.4	1.01(9)	9.4(4)	0.62(7)	2.80(3)	0.58(7)	6.56(3)	0.32(3)	60(10)	1.19(57)	1.73/2.19
50023-01-22-00	51695.33	2720	476.1	1.01(9)	8.6(2)	0.56(6)	3.02(4)	0.81(3)	6.59(4)	0.31(4)	60(10)	1.1(57)	1.82/2.22
50023-01-23-00	51697.45	2112	248	0.99(2)	7.8(3)	0.52(8)	2.89(6)	0.92(4)	6.68(6)	0.23(5)	40(10)	0.89(57)	1.83/2.14
50023-01-24-00	51709.69	2560	188.5	0.97(4)	9.5(6)	0.7(2)	1.96(3)	0.5(2)	6.64(5)	0.30(4)	40(10)	1.29(57)	1.38/1.83
50023-01-25-00	51712.35	2672	803.3	0.90(4)	7.8(2)	0.30(1)	2.63(4)	1.8(5)	6.72(3)	0.19(2)	30(10)	1.09(57)	1.56/1.84
50023-01-26-00	51715.41	2528	576.4	0.99(7)	13.8(7)	0.51(4)	2.36(3)	0.8(3)	6.59(4)	0.16(2)	30(10)	1.19(57)	1.52/2.26
50023-01-27-00	51718.93	3024	655.6	0.99(3)	9.9(5)	0.7(1)	2.58(5)	0.61(6)	6.67(3)	0.24(2)	40(10)	0.95(57)	1.72/2.28
50023-01-28-00	51721.86	2880	238.6	1.00(2)	9.3(3)	0.6(1)	2.54(4)	0.61(4)	6.56(4)	0.35(2)	50(6)	1.07(57)	1.74/2.23

Table 4
(Continued)

Observational ID	Start Time (MJD)	Exposure Time (s)	Rate (count s^{-1})	$\alpha = \Gamma - 1$	T_e (keV)	$\log(A)$[b]	N_{COMPTB}[c]	N_{Bbody}[c]	E_{line} (keV)	N_{line}[c]	EW_{line} (eV)	χ^2_{red} (dof)	F_1/F_2[d]
50023-01-29-00	51724.57	3344	1063	0.99(3)	5.92(9)	0.27(9)	3.4(1)	1.7(2)	6.57(3)	0.28(2)	50(10)	1.1(57)	2.13/1.71
50023-01-30-00	51727.50	3088	950.2	0.99(2)	6.4(2)	0.24(7)	3.1(1)	2.1(3)	6.71(3)	0.16(2)	30(10)	1.18(57)	1.90/1.62
50023-01-31-00	51730.42	2768	226	0.99(4)	6.7(3)	0.3(1)	2.62(8)	0.9(1)	6.58(5)	0.28(5)	40(10)	1.02(57)	1.71/1.59
50023-01-32-00	51733.41	2912	817.7	1.0(2)	3.7(1)	0.2(1)	3.4(1)	1.9(2)	6.61(4)	0.35(4)	50(8)	1.05(57)	1.36/1.11

Notes. The count rate corresponds to 5 PCA units and corrected for background. Parameter errors correspond to the 1σ confidence level.
[a] The spectral model is *wabs* ∗ (*blackbody* + *COMPTB* + *Gaussian*), where N_H is fixed at a value 2.73×10^{22} cm^{-2} (Piraino et al. 2000); color temperatures T_s and T_{BB} are fixed at 1.3 and 0.7 keV, respectively (see comments in the text).
[b] When parameter $\log(A) \gg 1$, it is fixed at 1.0 (see comments in the text).
[c] Normalization parameters of *blackbody* and *COMPTB* components are in units of L_{37}/d_{10}^2 erg^{-1} s^{-1} kpc^{-2}, where L_{37} is the source luminosity in units of 10^{37} erg s^{-1}, d_{10} is the distance to the source in units of 10 kpc, and the *Gaussian* component is in units of 10^{-2} × total photons cm^{-2} s^{-1} in line.
[d] Spectral fluxes (F_1/F_2) in units of $\times 10^{-9}$ ergs s^{-1} cm^{-2} for (3–10) and (10–60) keV energy ranges, respectively.

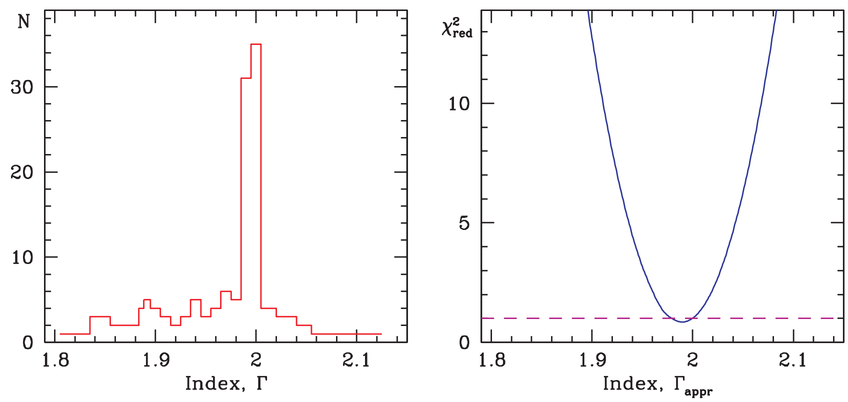

Figure 6. Left panel: histogram (frequency distribution) of the best-fit photon power-law index Γ obtained using a model *wabs* ∗ (*blackbody* + *COMPTB* + *Gaussian*) for *RXTE* data (1996–2000). Right panel: function $\chi^2(\Gamma_{appr}) = \frac{1}{N}\sum_{i=1}^{N}\left(\frac{\Gamma_i - \Gamma_{appr}}{\Delta\Gamma_i}\right)^2$ vs. Γ_{appr}. A dashed horizontal line indicates the critical residual level $\chi^2_{red} = 1$ (see comments in the text).
(A color version of this figure is available in the online journal.)

Figure 6. One can clearly see a sharp minimum of function $\chi^2_{red}(\Gamma_{appr})$ around 1, which takes place in the range of $\Gamma_{appr} = 1.99 \pm 0.01$ with a confidence level of 67% and $\Gamma_{appr} = 1.99 \pm 0.02$ with a confidence level of 99% for 127 dof.

It is important to emphasize that the photon index Γ is also independent of the luminosity of the blackbody component of *COMPTB* L_{39}/d_{10}^2 and the plasma temperature of Compton cloud T_e (see Figures 7 and 8).

Using *BeppoSAX* data FT11 suggested that the photon index Γ is about 2 for quite a few NS sources that are observed in the different spectral states. FT11 data characterize the spectral state by a value of electron temperature T_e and they show that $\Gamma = 2 \pm 0.2$ (or $\alpha = 1 \pm 0.2$) when kT_e changes from 2.5 to 25 keV.

A number of X-ray flaring episodes of 4U 1728-34 have been detected with *RXTE* during 1998–1999 (R3, R4 sets) and 2000 (R7, R8 sets) with good rise–decay coverage. We have searched for common spectral and timing features that can be revealed during these spectral transition episodes. We present the combined results of the spectral analysis of these observations using our spectral model *wabs* ∗ (*blackbody* + *COMPTB* + *Gaussian*) in Figures 9 and 10. The *RXTE*/ASM count rate is shown in the top panel. Further, from the top to the bottom, we show the model flux in two energy bands 3–10 keV (blue points) and 10–60 keV (crimson points). In the next panel we show a change of the TL electron temperature kT_e. One can clearly see the spectral transition from the HS to the LS during the time period from MJD 51070 to MJD 51215 when electron temperature kT_e varies from 3 keV to 15 keV. Normalizations of the *COMPTB* (crimson points) and *blackbody* components (blue points) are shown in the next panel of Figures 9 and 10. In particular, one can see from Figures 9 and 10 how *COMPTB* normalization N_{COMPTB} correlates with the variations of the ASM count rate and the model flux in the 3–10 keV energy band. On the other hand, the normalization of the *blackbody* component N_{BB} is almost constant except at the flaring episode peak, when N_{BB} increases from 0.09 to 0.27 (see blue points in Figure 9 at MJD = 51093 and 51133). Moreover, these flare spectral transitions are related to a noticeable increase in soft flux, in the energy range 3–10 keV, and decrease in hard flux, that in 10–60 keV (see the second panels from the top in Figures 9 and 10).

The spectral index α ($\alpha = \Gamma - 1$) is presented in the bottom panels of Figures 9 and 10. The index α slightly varies around 1 (or $\Gamma \sim 2$). Photon index Γ variation over the entire set of the observations is presented in Figure 6. The electron temperature kT_e steadily decreases during the burst rise (see blue vertical strips in Figures 9 and 10). Equivalent width of iron line EW_{line} and the normalizations of *COMPTB* N_{COMPTB} and blackbody components N_{BB} steadily increase when the electron temperature decreases (see Figure 11).

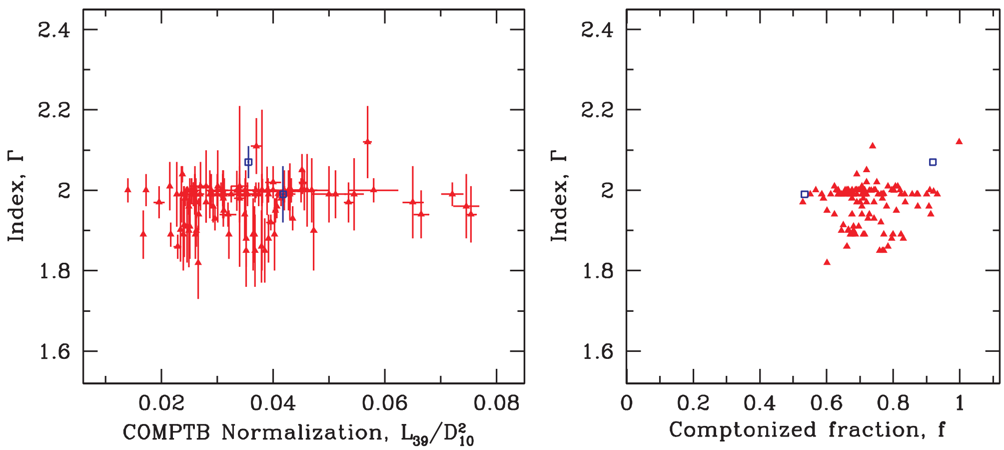

Figure 7. Plotted on the left is photon index Γ vs. *COMPTB* normalization $N_{\rm COMPTB} = L_{39}/D_{10}^2$ and on the right that vs. Comptonized fraction $f = A/(1 + A)$ using our spectral model *wabs* ∗ (*blackbody* + *COMPTB* + *Gaussian*) (see details in Tables 3 and 4). Blue and red points correspond to *BeppoSAX* and *RXTE* observations of 4U 1728-34, respectively.

(A color version of this figure is available in the online journal.)

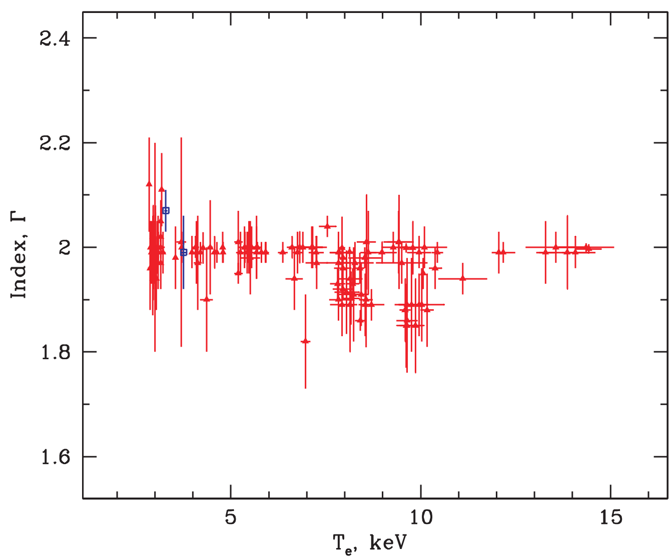

Figure 8. Photon index plotted vs. electron temperature T_e (in keV) in the framework of our spectral model *wabs* ∗ (*blackbody* + *COMPTB* + *Gaussian*) (see details in Tables 3 and 4). Blue and red points correspond to *BeppoSAX* and *RXTE* observations of 4U 1728-34, respectively.

(A color version of this figure is available in the online journal.)

In fact, a decrease in electron temperature T_e of the Compton cloud (TL) with an increase in the (disk) soft flux is a well-known effect, explained in detail by Titarchuk et al. (1998) and Titarchuk & Fiorito (2004).

As shown on the right-hand panel of Figure 7, the Comptonization fraction f varies from 0.6 to 0.9. This means that in most cases the soft disk radiation of 4U 1728-34 is subjected to reprocessing in the Compton cloud, and only a small fraction of the disk emission component $(1 - f)$ is directly seen by the Earth observer. Thus, the energy spectrum of 4U 1728-34 during all states is dominated by a Comptonized component, while the direct disk emission is always weaker and detectable in the flaring episodes only (see Figures 9 and 10).

Note that for BHs a definition of spectral transition is related to a change in photon index Γ (see, e.g., ST09). However, there is no one-to-one correspondence between Γ and cutoff (or *e*-fold) energy $E_{\rm fold}$. Titarchuk & Shaposhnikov (2010) demonstrate using *RXTE* data for BH binary XTE J1550−564 that $E_{\rm fold}$ decreases when Γ increases from 1.4 to 2.1 − 2.2 until Γ reaches 2.2 and then $E_{\rm fold}$ increases. Thus, for a BH the main parameter used for the spectral transition definition is a variable photon index Γ, which monotonically increases when a BH source goes to the HS.

It is important to emphasize once again that in the NS binary 4U 1728-34 the transition from the LS to the HS takes place when the electron (plasma) temperature changes from 15 keV to 2.5 keV. Thus, following the FT11 suggestion, we define the spectral state transition in an NS source in terms of the electron temperature T_e of the Compton cloud (TL). In this case the LS is characterized by high electron temperature T_e, while the HS is related to low T_e. Note that the electron temperature T_e is a directly measurable quantity, and it corresponds to cutoff energy of the spectrum.

Not all NSs show flares. Only a few NS binaries (such as *Z* and atoll sources) display spectral transitions during the bursts. Atoll sources, such as 4U 1728-34, usually show the flare transitions. One can establish a substantial difference between NSs and BHs due to these flare episodes when a source evolves from the LS to the HS and when plasma temperature of the Comptonized region changes remarkably (like in 4U 1728-34 from 2.5 keV to 15 keV). Thus, the NS low-mass X-ray binary 4U 1728-34 shows a steady decrease in electron temperature T_e from the LS to the HS, while the photon index Γ stays around 2. In contrast, in BH sources we see a steady monotonic growth of Γ, which is followed by its saturation (see, e.g., ST09).

5. CORRELATIONS BETWEEN SPECTRAL AND TIMING PROPERTIES DURING SPECTRAL STATE TRANSITIONS

The *RXTE* light curves have been analyzed using the *powspec* task from FTOOLS 5.1. The timing analysis *RXTE*/PCA data were performed in the 13–30 keV energy range using the *event* mode. The time resolution for this mode is 1.2×10^{-4} s. We generated power density spectra (PDS) in the 0.1–500 Hz frequency range with a 0.001 s time resolution. We subtracted the contribution due to Poissonian statistics. To model PDS we used QDP/PLT[12] plotting package.

[12] http://heasarc.gsfc.nasa.gov/ftools/others/qdp/qdp.html.

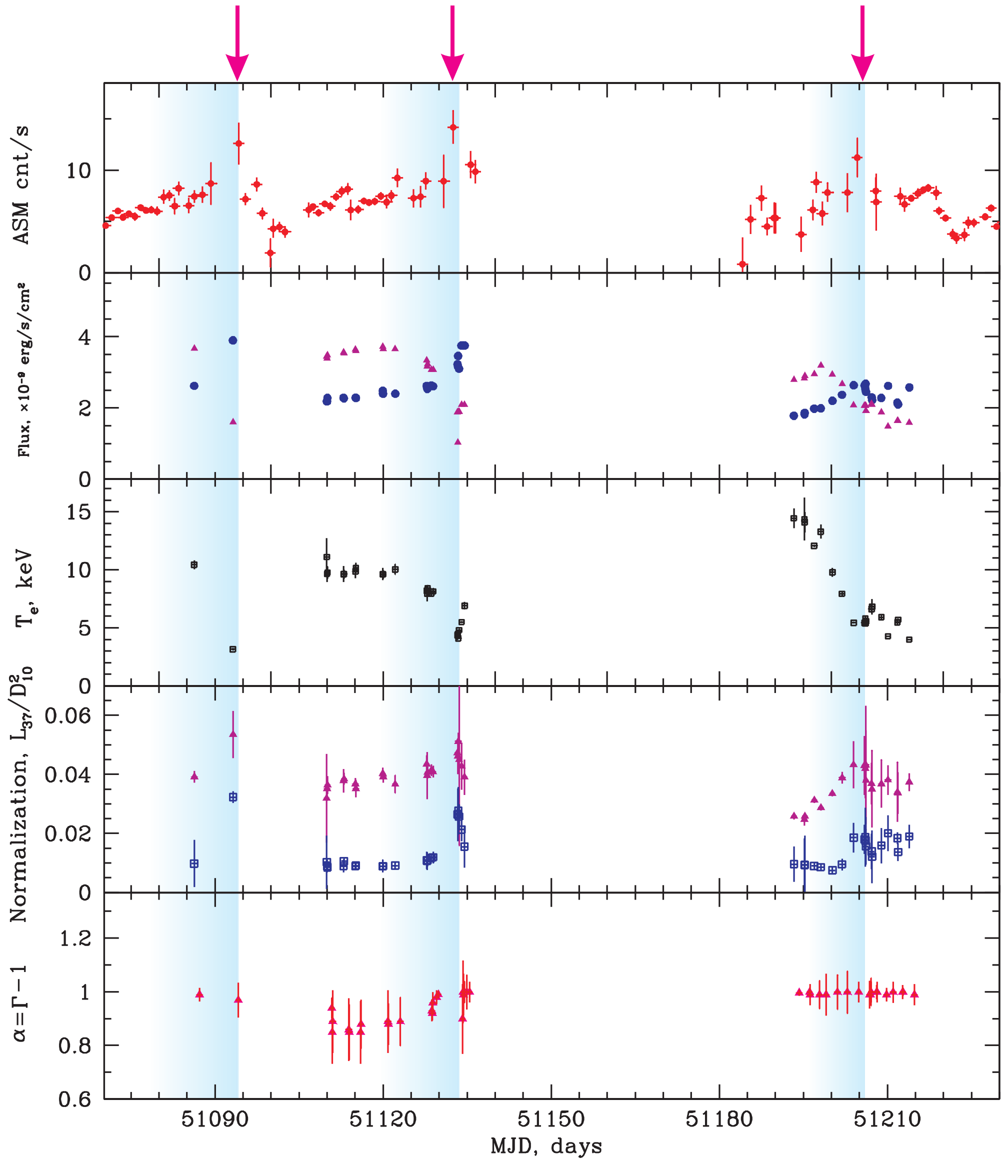

Figure 9. From top to bottom: evolution of the *RXTE*/ASM count rate, model flux in 3–10 keV and 10–60 keV energy ranges (blue and crimson points, respectively), electron temperature kT_e in keV, and *COMPTB* and *blackbody* normalizations (crimson and blue, respectively) during 1998 and 1999 flare transition set (R3, R5). In the last bottom panel, we present an evolution of the spectral index $\alpha = \Gamma - 1$. The rising phases of the burst are marked with blue vertical strips. The peak burst times are indicated by the arrows at the top of the plot.

(A color version of this figure is available in the online journal.)

Previously, timing analysis of 4U 1728-34 was carried out by Di Salvo et al. (2001) as a function of source position in a color–color diagram for *RXTE* data (R1, R2 sets in our terms). In the island part of the color–color diagram (corresponding to the hardest energy spectra), the power spectrum of 4U 1728-34 shows several features such as a band-limited noise component presented up to a few tens of Hz, a low frequency quasi-periodic oscillation (LFQPO) at frequencies between 20 and 40 Hz, a peaked noise component around 100 Hz, and one or two QPOs at kHz frequencies. During burst evolution (moving along the color–color diagram) in the lower banana (corresponding to the softer energy spectra) they found a very low frequency noise (VLFN) component below ∼1 Hz. In the upper banana (corresponding to the softest energy spectra) the power spectra are dominated by the VLFN with a peaked noise component around 20 Hz.

We find a similar timing behavior of 4U 1728-34 in our data set along with the energy spectra. In particular, in Figure 12, we show the details of a typical evolution of X-ray timing and spectral characteristics during X-ray flares. The evolution of the *RXTE*/ASM count rate during the 1998 (R3) outburst transition is presented at the top. Red/blue points A, B, and C mark moments at MJD = 51122/51128, 51133.27/51133.34, and 51196/51193 before, during, and after the X-ray outburst, respectively. In the lower panels (left column) we show PDSs for the 13–30 keV energy band along with the energy spectral diagram $E * F(E)$ (right column) for A (top), B (middle), and C (bottom) points of the X-ray light curve. The strong noise components with a break at 1–3 Hz and broad QPOs centered in the range 7–10 Hz are seen before and after the burst, but the latter feature is not seen at the B moment (see panel B1), i.e., at the X-ray flare peak. During the B1-burst event one can

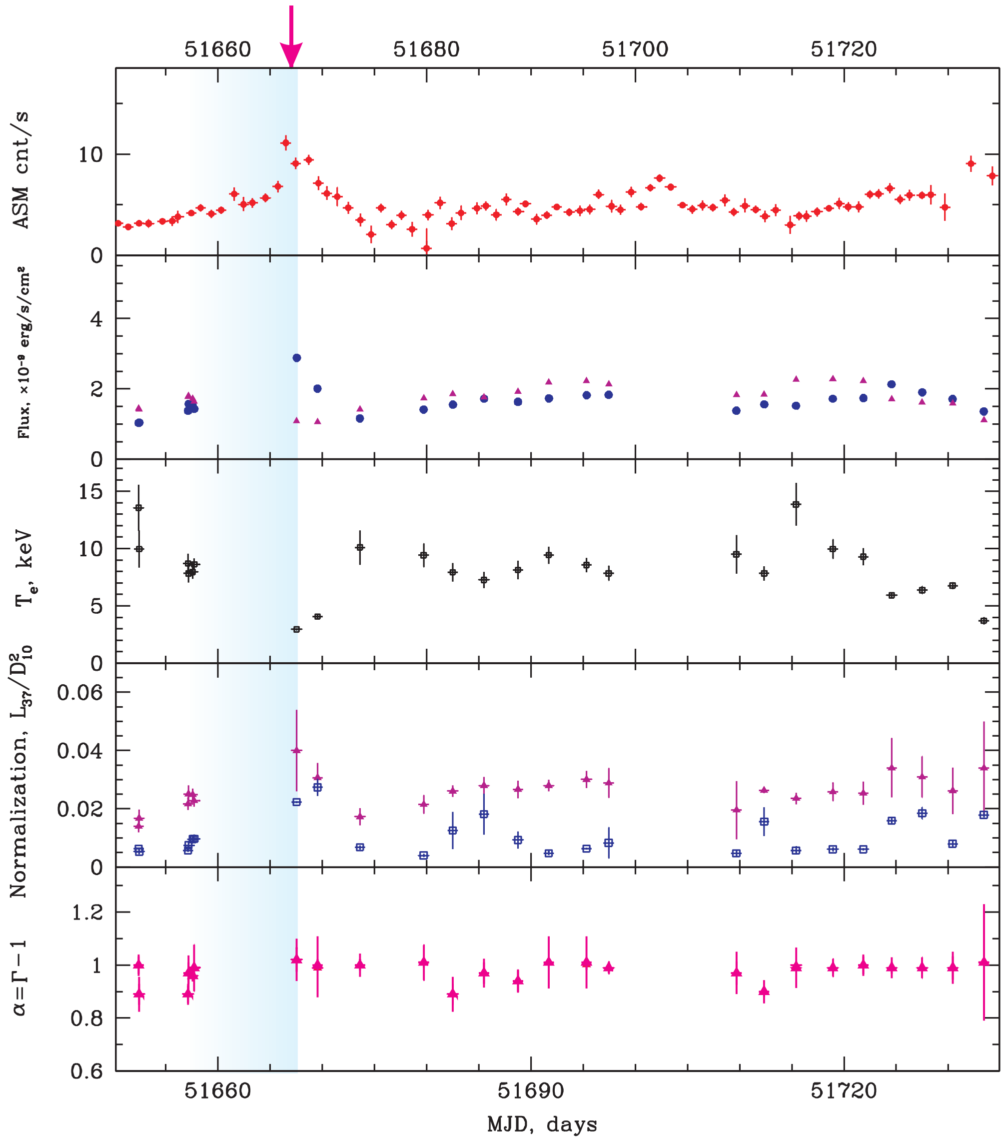

Figure 10. Similar to that presented in Figure 9 but for the *RXTE* 2000 flare transition set (R7, R8).

(A color version of this figure is available in the online journal.)

see a noise component with the power peak shifted to higher frequency with respect to that at A1/C1 events. In other words, the burst power spectrum, in this case, consists of the "high frequency" white–red noise component with a break at ∼40 Hz. On the right-hand side we present the $E*F(E)$ spectral diagrams (panels A2, B2, and C2) related to the corresponding power spectra (panels A1, B1, and C1). The data are shown by red points, and the spectral model components are displayed by blue, black, and dashed purple lines for *COMPTB*, *blackbody*, and *Gaussian* components, respectively.

Specifically, before the burst (A1 red; the 30042-03-08-00 *RXTE* observation, MJD = 51122) one can see a broken power-law noise component with a break at 1 Hz, broad QPO at 20 Hz (described by Lorentzian with FWHM = 11.7 ± 4.5 Hz, rms = 6.3 ± 1.0%, χ^2 =131 for 102 dof for a 67% confidence level). Later, just before the burst (A1 blue; 30042-03-11-00, MJD = 51128), break frequency of the broken power-law noise component shifts from 1 Hz to 3 Hz and QPO becomes less evident, but still visible at the 10–20 Hz range. The low-frequency part of the $\nu \times$ *power* diagram below 1 Hz increases right before the burst (A1, blue). During the burst (B1 red, 30042-03-14-02, MJD = 51133.27; B1 blue, 30042-03-14-01, MJD = 51133.34) one can see a white–red noise component with the break frequency shifted to higher frequency at about 40 Hz. The QPO component is not seen in the power spectrum during the burst at frequencies 80 Hz and lower.

We should point out once again that a similar behavior of 4U 1728-34 was detected previously by Di Salvo et al. (2001) during the 1996–1997 transition from island to banana states in the color–color diagram which we call a "burst" transition in this paper. Note that according to Di Salvo et al. (2001) the power spectrum at the upper banana state (at the maximum of the burst) consists of two noise components, namely, VLFN and high frequency noise (HFN). In addition, we have detected a particular burst when the power spectrum is presented only with a single HFN component (see panel (B1) of Figure 12).

After the outburst (C1 blue, 30042-03-18-00, MJD = 51193; C1 red, 30042-03-20-00, MJD = 51196) one can see the same features in the $\nu \times$ *power* plot as in that before the burst, but

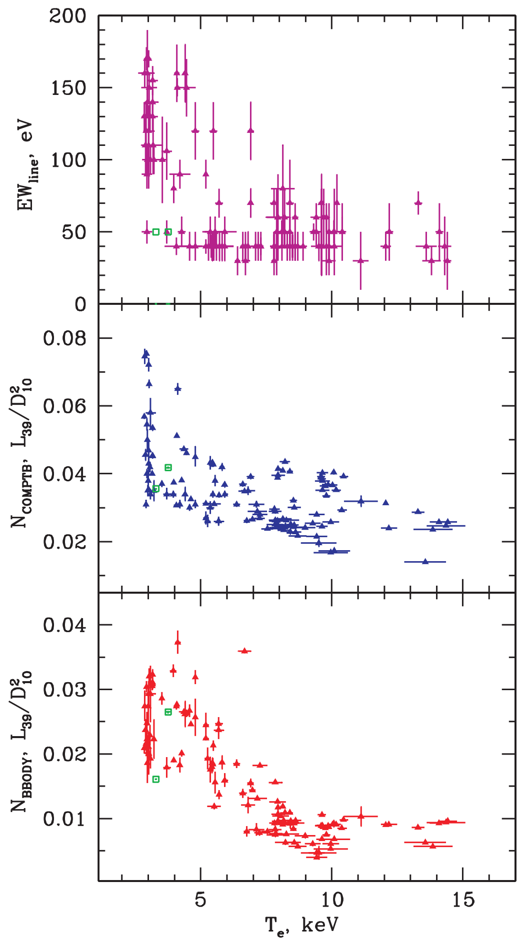

Figure 11. Equivalent width of the iron line (in eV, top), normalizations of *COMPTB* (middle) and *Blackbody* (bottom) components plotted vs. electron temperature T_e (in keV) in the framework of our spectral model *wabs* ∗ (*blackbody* + *COMPTB* + *Gaussian*) during flare transitions (see also Tables 3 and 4). Green points correspond to *BeppoSAX* observations of 4U 1728-34.

(A color version of this figure is available in the online journal.)

with slightly different parameters: $\nu_{br} \sim 1$, 2 Hz and $\nu_{QPO} \sim 6$, 10 Hz (described by Lorenzian with FWHM $= 6.0 \pm 2.1/15.0 \pm 2.9$ Hz, rms $= 8.1 \pm 0.4/10.6 \pm 1.4\%$, and $\chi^2 = 139/143$ for 102 dof; all parameter errors correspond to the 1σ confidence level).

In Figure 13 we present the $\nu \times$ *power* plot observed on 2000 March 7 (the 50023-01-01-00 *RXTE* observation, MJD = 51610) during the quiet state in order to compare it with the typical sample of PDS during the X-ray flare event (see panel (B1) of Figure 12).

6. DISCUSSION

We show the quasi-constancy of the photon (spectral) index in quite a few observations of the NS source 4U 1728-34 using *BeppoSAX* and *RXTE* observations. In Figures 7 and 8 we present plots of the photon index Γ as functions of our model parameters: electron temperature T_e (in keV), the *COMPTB* normalization (which equals the normalization of NS blackbody seed photons), and the Comptonization fraction $f = A/(1 + A)$. We obtain these results using an application of the first principle spectral model to extensive *BeppoSAX* and *RXTE* observations of the NS binary source 4U 1728-34. FT11 give an explanation of this index stability, which was also revealed in other observations of NS binaries. In this paper, for the completeness of our presentation, we review the main points of the FT11 explanation in terms of the transition layer model.

The energy balance in the TL is dictated by Coulomb collisions with protons (gravitational energy release), while inverse Compton and free–free emission are the main cooling channels (see the formulation of this problem in the pioneer work by Zel'dovich & Shakura 1969 as well as a similar consideration in Bisnovatyi et al. 1980). In fact, for the characteristic electron temperature (3 keV $\lesssim kT_e \lesssim 30$ keV) and density values ($\lesssim 10^{-5}$ g cm^{-3}) of these regions in low-mass X-ray binaries, Compton cooling dominates over free–free emission; the relation between the energy flux per unit surface area of the corona $Q_{\rm cor}$, the radiation energy density $\varepsilon(\tau)$, and electron temperature T_e is given by (see also Titarchuk et al. 1998)

$$\frac{Q_{\rm cor}}{\tau_0} \approx 20.2\varepsilon(\tau)T_e(\tau), \tag{1}$$

where τ_0 is the Thomson optical depth of the TL. The distribution $\varepsilon(\tau)$ is obtained as a solution of the diffusion equation

$$\frac{d^2\varepsilon}{d\tau^2} = -\frac{3Q_{\rm tot}}{c\tau_0}, \tag{2}$$

where $Q_{\rm tot} = Q_{\rm cor} + Q_{\rm disk}$ is the sum of the corona (TL) and intercepted disk fluxes, respectively. Combination of Equation (2) with two boundary conditions at the NS surface and the outer TL boundary leads us to the formulation of the TL boundary problem (see details in FT11). The solution for $\varepsilon(\tau)$ is then given by

$$\varepsilon(\tau) = \frac{2Q_{\rm tot}}{c}\left[1 + \frac{3}{2}\tau_0\left(\frac{\tau}{\tau_0} - \frac{\tau^2}{2\tau_0^2}\right)\right]. \tag{3}$$

In order to establish the average plasma temperature T_e we estimate the mean energy density in the TL as

$$\langle\varepsilon(\tau)\rangle = \frac{1}{\tau_0}\int_0^{\tau_0}\varepsilon(\tau)d\tau = \frac{Q_{\rm tot}}{c}(2 + \tau_0). \tag{4}$$

If we now substitute the result of Equation (4) into Equation (1), after a bit of straightforward algebra we obtain

$$\frac{kT_{\rm e}\tau_0(2 + \tau_0)}{m_ec^2} = \frac{0.25}{1 + Q_{\rm disk}/Q_{\rm cor}}. \tag{5}$$

One should use a formula for spectral index α

$$\alpha = -\frac{3}{2} + \sqrt{\frac{9}{4} + \frac{\beta}{\Theta}}, \tag{6}$$

where $\Theta \equiv kT_{\rm e}/m_ec^2$, and the β-parameter is as defined in Titarchuk & Lyubarskij (1995). If we replace β with its diffusion limit $\beta_{\rm diff}$

$$\beta_{\rm diff} = \frac{1}{\tau_0(2 + \tau_0)} \tag{7}$$

and using Equation (5), we obtain the diffusion spectral index as

$$\alpha_{\rm diff} = -\frac{3}{2} + \sqrt{\frac{9}{4} + \frac{1 + Q_{\rm disk}/Q_{\rm cor}}{0.25}}, \tag{8}$$

or $\alpha_{\rm diff} \approx 1 + 0.8Q_{\rm disk}/Q_{\rm cor}$ and

$$\Gamma_{\rm diff} \approx 1 + \alpha_{\rm diff} = 2 + 0.8Q_{\rm disk}/Q_{\rm cor} \tag{9}$$

for $Q_{\rm disk}/Q_{\rm cor} < 1$.

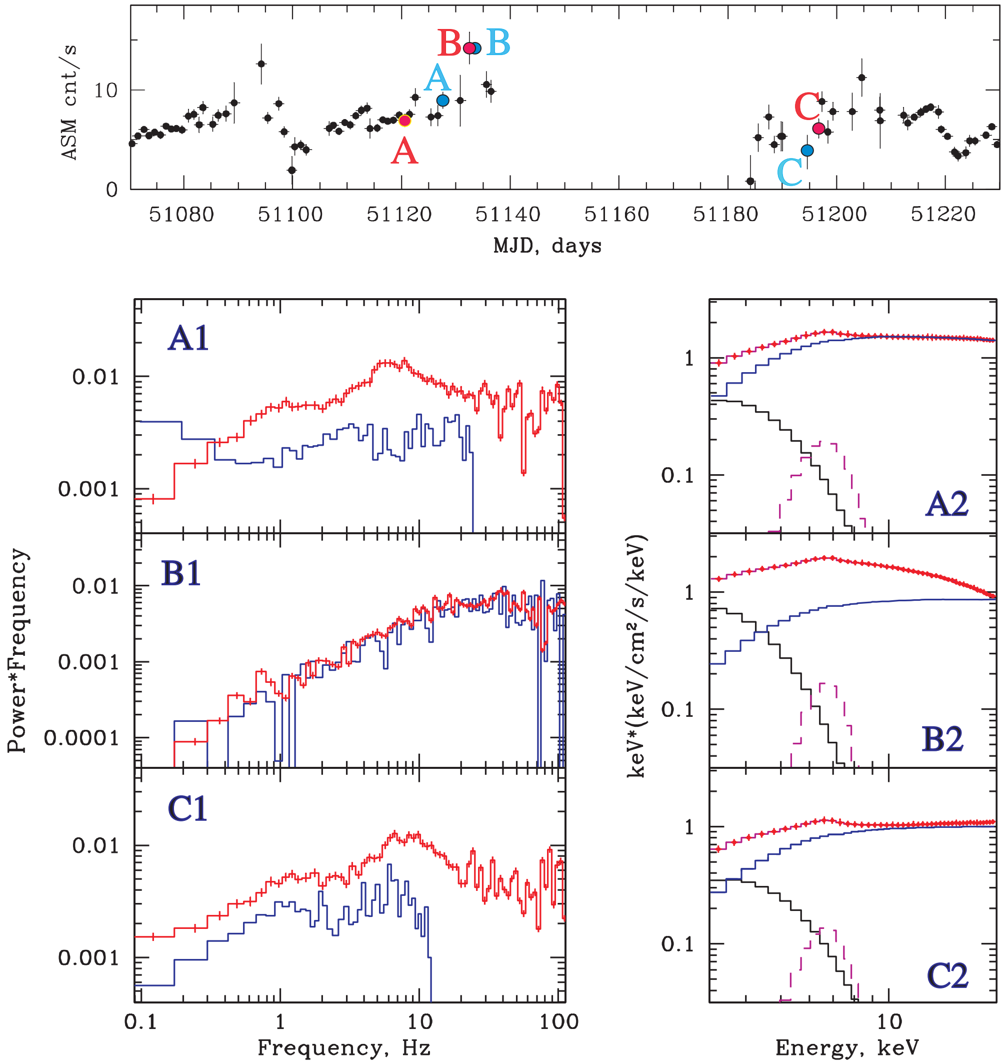

Figure 12. Upper panel: *RXTE*/ASM count rate during the 1998–1999 (R3, R5) outburst transition. Red/blue points A, B, and C mark moments at MJD = 51122/51128, 51133.27/51133.34, and 51196/51193 (before, during, and after X-ray outburst, respectively). Lower panels: PDSs for the 13–30 keV energy band (left column) are plotted along with energy spectral diagram $E * F(E)$ (right column) related to the A, B, and C points of the X-ray light curve (upper panel). The strong noise component related to the break at 1–3 Hz and broad QPOs centered at 7–10 Hz are present before and after the burst (see panels (A1) and (C1)). At the X-ray flare peak (see panel (B1)) one can see a white–red noise PDS with the break at about 40 Hz. On the right-hand side panels we present the $E * F(E)$ spectral diagrams (panels A2, B2, and C2) related to the corresponding power spectra (panels A1, B1, and C1). The data are shown by red points, and the spectral model components are displayed by blue, black, and dashed purple lines for *COMPTB*, *blackbody*, and *Gaussian* components, respectively.

(A color version of this figure is available in the online journal.)

Thus, until $Q_{\rm disk}/Q_{\rm cor} \ll 1$ photon index $\Gamma \approx 2$. This is precisely what we see in the observations of NS 4U 1728-34 (see Figures 6–8).

However, in BHs we observe that the photon index monotonically increases with QPO frequency and the mass accretion rate and finally saturates (see ST09, TS09, and ST10). Recently, Laurent & Titarchuk (2011), hereafter LT11, made Monte Carlo simulations of X-ray spectral formation in the Compton cloud that surrounds a BH. They reproduced the observed correlation index versus mass accretion rate. They also demonstrated that the index saturation observed in BH sources is a result of two effects, namely, cooling of the CF by the soft disk photons along with the photon capture by a BH. In fact, spectral index is the inverse of the Comptonization parameter Y, which is proportional to mean number of upscattering N_{sc} and efficiency of upscattering η. But in the relatively cold CF photons (when mass accretion rate $\dot{m}$ in Eddington units is much greater than 1) mostly upscatter of electrons in the direction of the flow for which N_{sc} is proportional to CF optical depth $\tau_{\rm CF}$ (or $\dot{m}$) and η is inverse proportional to $\tau_{\rm CF}$ ($\dot{m}$). Thus, the spectral (photon) index saturates when the mass accretion rate increases. This is precisely what was reproduced in the MC simulations by LT11. Hence, one can conclude that the monotonic growth of the photon index Γ with the mass accretion rate followed by its saturation is the observational signature of a BH while the constancy of Γ (around 2) versus $\dot{m}$ (or electron temperature) is the NS signature.

Recently Soria et al. (2011) found that in ultra luminous X-ray source HLX1 photon index changes from 1.8 to 2.95 but they were unable to find an argument as to whether this source is intermediate-mass BH or foreground NS. Comparison of our and FT11 results for NSs and ST09 results for BHs (see also LT11) indicates that HLX1 is probably a BH because its photon index changes in the wide range from 1.8 to 2.95 (see Figure 14) but in an NS case the index does not vary and has almost a constant value around 2 (see Figures 6–8).

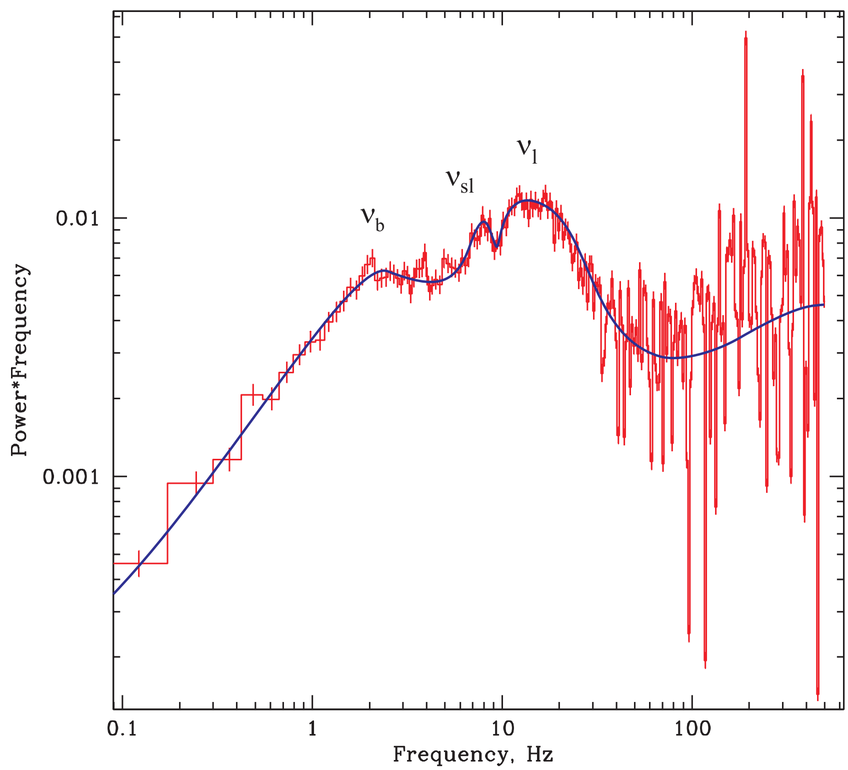

Figure 13. $\nu \times power$ diagram of 4U 1728-34 in the 0.1–150 Hz range, observed on 2000 March 7 (50023-01-01-00, MJD = 51610). The blue solid line shows the best fit of the power spectrum, which typically consists of three components: the broadband noise with break ν_b (broken power law), low-frequency QPOs fit by Lorentzians (ν_{sl}, ν_l), and ~100 Hz bump noise (see Di Salvo et al. 2001).

(A color version of this figure is available in the online journal.)

7. SUMMARY

We presented our analysis of the spectral properties observed in X-rays from the NS X-ray binary 4U 1728-34 during transitions between the LS and the HS. We analyzed a number of transition episodes from this source observed with *BeppoSAX* and *RXTE* satellites. For our analysis we used a good spectral coverage and resolution of *BeppoSAX* detectors from 0.1 to 200 keV along with extensive *RXTE* observations in the energy range from 3 to 60 keV.

We show that the X-ray broadband energy spectra during all spectral states can be adequately fitted by the composition of the *Blackbody*, Comptonized component (*COMPTB*), and *Gaussian* component. We also show that photon index Γ of the best-fit Comptonized component in 4U 1728-34 is almost constant, about 2 (see Figure 6) and consequently almost independent of *COMPTB* normalization L_{39}/D_{10}^2, which is proportional to the disk mass accretion rate $\dot{m}$, (see the left-hand panel of Figure 7) and plasma temperature of Compton cloud T_e (see Figure 8). Note the soft (disk) photon luminosity L_{39} is in units of 10^{39} erg s^{-1} and the distance to the source D_{10} is in units of 10 kpc. This index stability has been recently suggested using a quite a few number of other NS sources, Cyg X-2, Sco X-1, GX 17+2, GX 340+0, GX 3+1, GX 349+2, X 1658-298, GS 1826-238, and 1E 1724-3045, which were observed by *Beppo*SAX at different spectral states (see details in FT11).

A relatively high value of Comptonized fraction $f = 0.6$–0.9, obtained in the framework of our spectral model, indicates significant reprocessing of X-ray disk emission in the Compton cloud in 4U 1728-34.

Using *BeppoSAX* observations, we also find that there are two sources of blackbody emission. One is presumably related to the accretion disk, and the other is related to the NS surface, for which temperatures of soft photons are about 0.7 keV and 1.3 keV, respectively.

We demonstrate that the photon index $\Gamma \sim 2$ is almost constant when the source moves from the LS to the HS, i.e., when the plasma temperature of the Comptonized region varies from 15 to 2.5 keV (see Figure 8).

We present strong theoretical arguments that the dominance of the energy release in the TL with respect to the soft flux coming from the accretion disk, $Q_{\rm disk}/Q_{\rm cor} \ll 1$, leads to almost constant photon index $\Gamma \approx 2$.

Thus, we argue that this index stability is the intrinsic signature of an NS binary source, while in BHs the index monotonically changes with the mass accretion rate and ultimately saturates (see ST09). In Figure 14 we demonstrate the index correlation versus mass accretion rate for a number of BH sources and that the index depends on the mass accretion rate in NS 4U 1728-34. Photon indices of BHC sources (GRS 1915+105, GX 339-4, SS 433, and GRO J1655-40) show clear correlation with mass accretion rate $\dot{m}$ or with soft photon normalization L_{39}/D_{10}^2, which is proportional to $\dot{m}$. This correlation is followed by the index saturation when $\dot{m}$ exceeds a certain level. The behavior of the index for the considered NS 4U 1728-34 is clearly different from that for the sample of BHC sources.

We thank Chris Shrader and Cristiano Guidorzi for careful reading and editing of this paper. We are very grateful to the

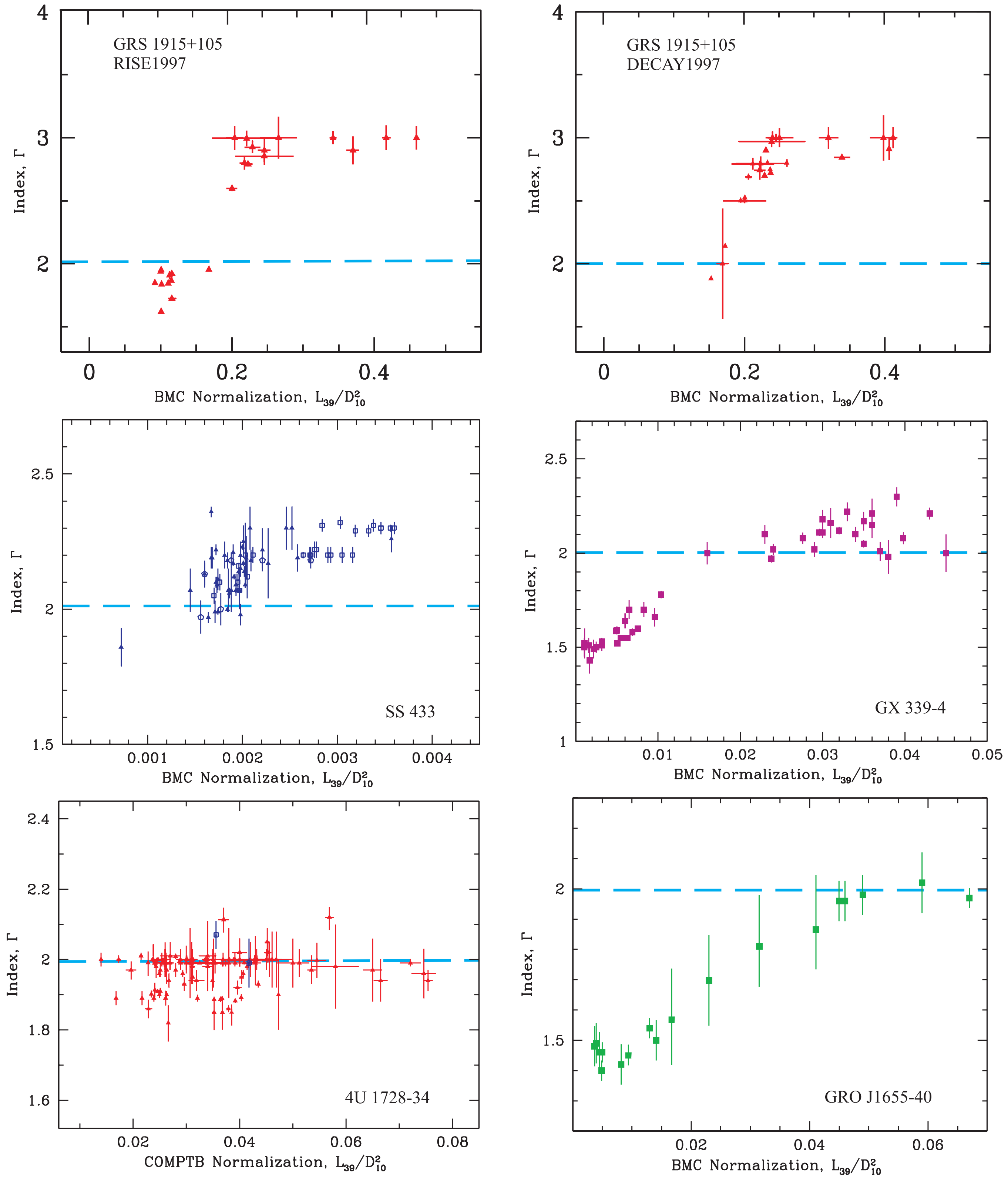

Figure 14. Examples of diagrams of photon index Γ vs. mass accretion rate for BHC sources (GRS 1915+105 (taken from TS09), GX 339-4 (ST08), SS 433 (ST10), and GRO J1655-40 (ST08)) along with that for atoll NS 4U 1728-34. One can see a noticeable change of Γ followed by saturation plateau for BHs as for NS 4U 1728-34 the index slightly varies about 2 (see also Figure 6). The level for $\Gamma = 2$ is indicated by the blue dashed line.

(A color version of this figure is available in the online journal.)

referee for his/her valuable comments and corrections to the content of this paper. L.T. acknowledges the support of this paper by the ADP NASA grant, NNX09AF02G.

APPENDIX

ON THE DEFINITION OF THE NORMALIZATION OF THE *COMPTB* AND *BMC* MODELS

The *COMPTB* and *BMC* models describe the outgoing spectrum as a convolution of the input "seed" blackbody-like spectrum, whose normalizations are $N_{\rm COMPTB}$ and $N_{\rm BMC}$ and color temperature is kT, with Comptonization Green's function. Similar to the ordinary *bbody* XSPEC model, bolometrical luminosity

$$L_{\rm bol} = \int_0^{\infty} E \times A(E) dE, \qquad \text{(A1)}$$

where $A(E)$ is the photon flux density of blackbody radiation

$$A(E) = 8.052 \times K \times \frac{E^2}{(kT)^4} \times \left(\exp \frac{E}{kT} - 1\right)^{-1}, \qquad \text{(A2)}$$

and $K = N_{\rm COMPTB} N_{\rm BMC}$ is the normalization of the seed blackbody photon spectrum, defined in the same way as the XSPEC *bbody* model.

Thus, one can calculate the emergent luminosity of the source as an integral

$$L_{\rm bol} = 8.052 \times K \int_0^{\infty} \frac{z^3 dz}{e^z - 1} = 8.052 \times K \times \frac{\pi^4}{15}. \qquad \text{(A3)}$$

On the other hand $N_{\rm BMC}, N_{\rm COMPTB} = K = L_{39}/D_{10}^2$ (see Section 6.2.10 of "User's Guide of an X-Ray Spectral Fitting Package XSPEC v.12.6.0"[13] and Farinelli et al. 2008[14]), where L_{39} is the source luminosity in units of 10^{39} erg s^{-1} and D_{10} is the distance to the source in units of 10 kpc. If we know K we can find L_{39} having D_{10}. Thus, similar to the ordinary *bbody* XSPEC model, the normalizations $N_{\rm COMPTB}$ and $N_{\rm BMC}$ are a ratio of the source (disk) luminosity to the square of the distance:

$$N_{\rm BMC}, N_{\rm COMPTB} = \left(\frac{L}{10^{39}\,{\rm erg\,s^{-1}}}\right)\left(\frac{10\,{\rm kpc}}{D}\right)^2. \qquad \text{(A4)}$$

This implies an important property of both *COMPTB* and BMC models. Namely, using these models one can correctly evaluate the normalization of the original "seed" component, which is presumably a correct mass accretion rate indicator.

REFERENCES

Basinska, E. M., Lewin, W. H. G., Sztajno, M., & Cominsky, L. R. 1984, ApJ, 281, 337
Bisnovatyi, G. S., Khlopov, M. Yu., Chechetkin, V. M., & Eramzhyan 1980, SvA, 24, 716
Boella, G., Chiappetti, L., Conti, G., et al. 1997, A&AS, 122, 327
Bradt, H. V., Rothschild, R. E., & Swank, J. H. 1993, A&AS, 97, 355
Churazov, E., Gilfanov, M., Sunyaev, R., et al. 1997, Adv. Space Res., 19, 55
D' Ai, A. R., Iaria, R., Di Salvo, T., et al. 2006, A&A, 448, 817
Di Salvo, T., Iaria, R., Burderi, L., & Robba, N. R. 2000, ApJ, 542, 1034
Di Salvo, T., Iaria, R., Robba, N. R., & Burderi, L. 2006, Chin. J. Astron. Astrophys., 6, 183
Di Salvo, T., Mendez, M., van der Klis, M., Ford, E., & Robba, N. R. 2001, ApJ, 546, 1107
Ebisawa, K., Titarchuk, L., & Chakrabarti, S. K. 1996, PASJ, 48, 59
Egron, E., Di Salvo, T., Burderi, L., et al. 2011, A&A, 530, A99
Farinelli, R., & Titarchuk, L. 2011, A&A, 525, 102 (FT11)
Farinelli, R., Titarchuk, L., Paizis, A., & Frontera, F. 2008, ApJ, 680, 602 (F08)
Ford, E., & van der Klis, M. 1998, ApJ, 506, L39
Forman, W., Tananbaum, H., & Jones, C. 1976, ApJ, 206, L29
Franco, L. 2001, ApJ, 554, 340
Frontera, F., Costa, E., dal Fiume, D., et al. 1997, Proc. SPIE, 3114, 206
Galloway, D. F., Muno, M. P., Hartman, J. M., Psaltis, D., & Chakrabarty, D. 2008, ApJS, 179, 360
Hoffman, J. A., Lewin, W. H. G., Doty, J., et al. 1976, ApJ, 210, L13
Hua, X.-M., & Titarchuk, L. 1995, ApJ, 449, 188
Jonker, P. G., Mendez, M., & van der Klis, M. 2000, ApJ, 540, L29
Kaminker, A. D., Pavlov, G. G., Shibanov, Y. A., et al. 1989, A&A, 220, 117
Kluzniak, W. 1993, A&AS, 97, 265
Kong, A. K. H., Charles, P. A., & Kuulkers, E. 1998, New Astron., 3, 301
Laurent, P., & Titarchuk, L. 1999, ApJ, 511, 289 (LT99)
Laurent, P., & Titarchuk, L. 2011, ApJ, 727, 34 (LT11)
Lewin, W. H. G., Clark, G., & Doty, J. 1976, IAU Circ., 2922, 1
Marti, J., Mirabel, I. F., Rodriguez, L. F., & Chaty, S. 1998, A&A, 332, L45
Mendez, M., van der Klis, M., & Ford, E. 2001, ApJ, 561, 1016
Migliari, S., van der Klis, M., & Fender, R. P. 2003, MNRAS, 345, L35
Ng, C., Daz, T. M., Cadolle, B. M., & Migliari, S. 2010, A&A, 522, A96
Oda, M., Gorenstein, P., Gursky, H., et al. 1971, ApJ, 166, L1
Parmar, A. N., Martin, D. D. E., Bavdaz, M., et al. 1997, A&AS, 122, 309
Piraino, S., Santangelo, A., & Kaaret, P. 2000, A&A, 360, L35
Remillard, R. A., & MacClintock, J. E. 2006, ARA&A, 44, 49
Reynolds, M. T., & Miller, J. M. 2011, ApJ, 734, L17
Seifina, E., & Titarchuk, L. 2010, ApJ, 722, 586 (ST10)
Shakura, N. I., & Sunyaev, R. A. 1973, A&A, 24, 337
Shaposhnikov, N., & Titarchuk, L. 2009, ApJ, 699, 453
Soria, R., Zampieri, L., Zane, S., & Wu, K. 2011, MNRAS, 410, 1886
Strohmayer, T. E., Zhang, W., Swank, J. H., et al. 1996, ApJ, 469, L9
Sunyaev, R. A., & Titarchuk, L. G. 1989, in Proc. 23rd ESLAB Symp. on Two Topics in X-Ray Astronomy, ed. J. Hunt & B. Batrick (ESA SP-296; Noordwijk: ESA), 627
Tennant, A. F., Fabian, A. C., & Shafer, R. A. 1986, MNRAS, 219, 871
Titarchuk, L. 1994, ApJ, 434, 570
Titarchuk, L., & Fiorito, R. 2004, ApJ, 612, 988
Titarchuk, L., Lapidus, I. I., & Muslimov, A. 1998, ApJ, 499, 315
Titarchuk, L., & Lyubarskij, Y. 1995, ApJ, 450, 876
Titarchuk, L., Mastichiadis, A., & Kylafis, N. D. 1997, ApJ, 487, 834
Titarchuk, L., & Seifina, E. 2009, ApJ, 706, 1463
Titarchuk, L., & Shaposhnikov, N. 2005, ApJ, 626, 298
Titarchuk, L., & Shaposhnikov, N. 2010, ApJ, 724, 1147
Titarchuk, L., & Zannias, T. 1998, ApJ, 493, 863
Titarchuk, L. G., & Osherovich, V. A. 1999, ApJ, 518, L95
van Paradijs, J. 1978, Nature, 274, 650
van Straaten, S., van der Klis, M., Kuulkers, E., & Mendez, M. 2001, ApJ, 551, 970
Zel'dovich, Ya. B., & Shakura, N. I. 1969, SvA, 13, 175

[13] https://heasarc.gsfc.nasa.gov/docs/software/lheasoft/xanadu/xspec/XspecManual.pdf
[14] http://heasarc.gsfc.nasa.gov/docs/xanadu/xspec/models/comptb.html